The correlation of dust and gas emission in star-forming environments

L. K. Morgan,[1][*] T. J. T. Moore,[1] D. J. Eden,[1] J. Hatchell[2] and J. S. Urquhart[3]

[1]*Astrophysics Research Institute, Liverpool John Moores University, IC2, Liverpool Science Park, 146 Brownlow Hill, Liverpool L3 5RF, UK*
[2]*Physics and Astronomy, University of Exeter, Stocker Road, Exeter EX4 4QL, UK*
[3]*Max-Planck-Institut für Radioastronomie, Auf dem Hügel 69, D-53121 Bonn, Germany*

ABSTRACT

We present ammonia maps of portions of the W3 and Perseus molecular clouds in order to compare gas emission with submillimetre continuum thermal emission which are commonly used to trace the same mass component in star-forming regions, often under the assumption of local thermodynamic equilibrium (LTE).

The Perseus and W3 star-forming regions are found to have significantly different physical characteristics consistent with the difference in size scales traced by our observations. Accounting for the distance of the W3 region does not fully reconcile these differences, suggesting that there may be an underlying difference in the structure of the two regions.

Peak positions of submillimetre and ammonia emission do not correlate strongly. Also, the extent of diffuse emission is only moderately matched between ammonia and thermal emission. Source sizes measured from our observations are consistent between regions, although there is a noticeable difference between the submillimetre source sizes with sources in Perseus being significantly smaller than those in W3.

Fractional abundances of ammonia are determined for our sources which indicate a dip in the measured ammonia abundance at the positions of peak submillimetre column density.

Virial ratios are determined which show that our sources are generally bound in both regions, although there is considerable scatter in both samples. We conclude that sources in Perseus are bound on smaller scales than in W3 in a way that may reflect their previous identification as low- and high-mass, respectively.

Our results indicate that assumptions of local thermal equilibrium and/or the coupling of the dust and gas phases in star-forming regions may not be as robust as commonly assumed.

Key words: methods: data analysis – stars: formation – stars: protostars – ISM: clouds – radio lines: ISM.

1 INTRODUCTION

In the study of star formation, the estimation of masses, temperatures and the internal gas velocity dispersions of protostellar and pre-stellar cores is fundamental to understanding the physical state of the core and hence to placing constraints on the processes of star formation and early stellar evolution. The submillimetre continuum emission from cool dust is regarded as the most reliable tracer of mass in cores, since its radiative transfer is simple and its abundance uncertainties relatively low. However, deriving the dust temperatures required for mass calculations from continuum measurements is not always straightforward, usually because of a lack of far-IR data with sufficient spatial resolution and sensitivity to match that available in the (sub)millimetre and mid-IR wavebands. In addition to this, acquiring kinematic information to determine,

e.g. the virial state of a core, requires spectroscopy of molecular emission lines that trace the denser core gas.

It is often assumed that the ammonia inversion transitions, with critical densities of a few $\times 10^3$ cm^{-3} (Maret et al. 2009), can be used to trace much the same mass component as the submillimetre continuum emission (e.g. Dunham et al. 2011; Urquhart et al. 2011) and, since the gas and dust should be in thermal equilibrium at densities typical of star-forming regions (10^5 cm^{-3} e.g. Keto & Caselli 2008), that both gas temperatures and line widths from NH$_3$ can be taken as representative of the dust-traced cores, allowing the calculation of core masses and virial ratios. This assumption is often necessary in order to perform virial analyses. However, there is evidence in the literature of the position of ammonia peaks failing to match the position of peaks of submillimetre emission (e.g. Zhou et al. 1991) and suggestions that NH$_3$ emission does not trace the densest gas in submillimetre cores (Friesen et al. 2009; Johnstone et al. 2010). Ammonia emission observed at the peak of submillimetre emission has also been noted to vary from measurements

[*] E-mail: lkm@astro.livjm.ac.uk

made at different positions within star-forming cores (Chira et al. 2013).

Several Green Bank Telescope (GBT) studies have been made of the NH_3 emission from protostellar cores in a number of Galactic star-forming regions and have been used to derive the important physical parameters of velocity dispersion and temperature in the dense gas of the core. One of these (Allsopp 2012) observed beam-spaced, 3×3 position grids centred on ~ 60 cores detected in the W3 star-forming giant molecular cloud in the 850 μm continuum by Moore et al. (2007). A surprising outcome of this study is that the cores appear to be poorly defined in NH_3 on scales of 1 arcmin (0.6 pc at the distance of W3), compared to the submillimetre continuum, in which they are compact with radii <30 arcsec. In contrast, no significant differences were found between grid centre and edge positions in the kinetic temperature, optical depth, column density, or velocity dispersion derived from NH_3 (Allsopp 2012). The simplest explanation for this is that the NH_3 emission is tracing a significantly larger and less dense gas component than the submillimetre continuum. Another major study, by Rosolowsky et al. (2008), observed NH_3 towards a selection of submillimetre-detected cores (among other positions described in the paper) in the Perseus (mainly low-mass) star-forming region. Only a single point per core was observed and so no spatial information is available in NH_3, but a comparison between the two studies shows some significant differences between the NH_3-traced cores in the two star-forming regions. For example, the Perseus cores have generally lower gas kinetic temperatures, higher NH_3 optical depths and column densities than in the high-mass star-forming regions of W3.

Through observation of fully sampled, extended maps of ammonia cores associated with submillimetre emission this paper explores the likelihood that NH_3 and submillimetre continuum emission trace different structures in terms of extent and their spatial distribution. A determination of the typical size of cores in the Perseus and W3 regions shows significant systematic differences between the regions. These differences potentially mean that the two emission mechanisms are not tracing the same mass component. This result casts doubt on the use of NH_3-derived gas temperatures to calculate clump/core masses from submillimetre continuum fluxes and NH_3 velocity dispersions in combination with continuum masses in calculating virial ratios.

2 OBSERVATIONS

2.1 Observational set up

Fully sampled maps in the NH_3 (1,1) and (2,2) rotational inversion transition lines were made using the newly commissioned *K*-band focal plane array (KFPA) in shared-risk time on the 100-m GBT, operated by the National Radio Astronomy Observatory.[1]

Observations were made over seven sessions from the 2010 December 16 to the 2011 March 28. Sky subtraction was attained through off-source measurements and flux calibration on the T_A^* scale was achieved through switching observations of a noise diode. Comparison with previous observations using the dual-feed *K*-band receiver indicates that absolute flux calibration is accurate to $\lesssim 20$ per cent.

Atmospheric opacity values (at zenith) were determined from local weather models, collated in the archive maintained by R.Maddalena.[2] A spectral bandpass of 50 MHz was used, incorporating both the NH_3 (1,1) and (2,2) rotational inversion transitions at ~ 23.69 GHz and ~ 23.72 GHz, respectively.

Each map was completed using the 'Daisy' pattern, consisting of a petal-shaped scan trajectory with continuous sampling. The oscillation period of the daisy scan is calculated for each map so that full sampling is achieved within a radius of 3.5 arcmin. Outside of this radius the integration time per map pixel is radially dependent, resulting in reduced signal-to-noise ratios towards the map edges. This is compensated for in the reduction process via weighting by effective integration time per pixel. The fiducial radius of each of our maps is then 3.5 arcmin, with some coverage (incompletely sampled) beyond this radius due to the size of the receiver array. Where necessary, some maps were mosaicked together so that complete, fully sampled coverage of all desired regions could be obtained. Sampling rates were set at 1 or 2 seconds per sample, dependent upon the source and observing conditions, where the oscillation period of the daisy scan was defined with four samples per beam. Typical (median) pointing offsets were ~ 4 arcsec and weather conditions were stable during all seven observing sessions. On two occasions (the 2011 January 13 and the 2011 March 7) snow in the GBT dish was a concern with regard to observing efficiency. Through calibrator observations and comparison with previous observations gain values were adjusted where appropriate and we have achieved an absolute flux calibration accuracy of better than 20 per cent.

Maps were centred on individual submillimetre continuum sources selected from the catalogues of Hatchell et al. (2005, 2007) for Perseus and Moore et al. (2007) for W3. Targets were chosen partly at random but also selected to include both clustered regions, so that single maps cover several neighbouring objects, and isolated sources. The degree to which the resulting samples are representative of the populations of both regions is examined in Section 3.3. A total of 13 maps were completed in Perseus and 15 in the W3 GMC, with some overlaps. The pointing centres, observation dates and total integration times of these maps are listed in Table 1.

2.2 Data reduction and LTE analysis

Individual feeds, i.e. time series data from each of the seven receivers, were reduced by running data through the GBT pipeline which calibrates the data and reconstructs spatial image cubes using reference scans and performing sky subtraction as appropriate.[3] The output cubes were produced with an angular pixel size of 6 arcsec (in comparison to the GBT beam size of 30 arcsec). The GBT pipeline uses Parseltongue[4] scripts to control AIPS tasks which produce images of the combined spectral data and removes a second-order spectral baseline. The mosaicking and weighting of overlapping mapping observations was performed as part of the GBT pipeline reductions.

The determination of optical depth, rotational temperature, kinetic temperature and excitation temperature from ammonia (1,1) and (2,2) spectra, assuming local thermodynamic equilibrium

---

[1] The National Radio Astronomy Observatory is a facility of the National Science Foundation operated under cooperative agreement by Associated Universities, Inc.

[2] http://www.gb.nrao.edu/~rmaddale/Weather/
[3] https://safe.nrao.edu/wiki/pub/Kbandfpa/KfpaReduction/kfpaDataReduceGuide-11Dec01.pdf
[4] http://www.radionet-eu.org/rnwiki/ParselTongue

Table 1. Pointing centres and observation dates for each mapped region.

Region	Pointing centre position RA (J2000)	Dec. (J2000)	Observation date	Total integration time (m)
Perseus				
Map 01	03:25:48.8	+30:42:24	20th Dec 2010	21
Map 02	03:27:40.0	+30:12:13	7th Mar 2011	21
Map 03	03:28:32.2	+31:11:09	6th Jan 2011	41
Map 04	03:28:42.6	+31:06:13	21st Dec 2010	21
Map 05	03:29:03.4	+31:14:58	20th Dec 2010	41
Map 06	03:29:10.3	+31:13:35	21st Dec 2010	21
Map 07	03:29:18.5	+31:25:13	6th Jan 2011	32
Map 08	03:32:17.5	+30:49:49	21st Dec 2010	21
Map 09	03:33:13.3	+31:19:51	28th Mar 2011	41
Map 10	03:33:15.1	+31:07:04	28th Mar 2011	41
Map 11	03:41:46.0	+31:57:22	5th Jan 2011	41
Map 12	03:43:57.8	+32:04:06	7th Mar 2011	41
Map 13	03:44:48.8	+32:00:29	7th Mar 2011	41
W3				
Map 01	02:19:53.1	+61:01:55	16th Dec 2010	41
Map 02	02:20:41.0	+61:09:42	14th Jan 2011	41
Map 03	02:21:04.0	+61:06:01	14th Jan 2011	41
Map 04	02:21:06.0	+61:27:28	20th Dec 2010	41
Map 05	02:21:41.0	+61:05:44	14th Jan 2011	41
Map 06	02:22:23.0	+61:06:12	14th Jan 2011	41
Map 07	02:23:28.6	+61:12:04	21st Dec 2010	41
Map 08	02:25:31.2	+62:06:20	16th Dec 2010	82
Map 09	02:25:37.7	+61:13:51	19th Dec 2010	41
Map 10	02:26:40.0	+62:07:00	29th Mar 2011	41
Map 11	02:26:44.6	+61:29:44	20th Dec 2010	41
Map 12	02:27:17.8	+61:57:14	21st Dec 2010	41
Map 13	02:28:00.0	+61:24:00	29th Mar 2011	41
Map 14	02:28:12.3	+61:29:40	19th Dec 2010	41
Map 15	02:28:26.2	+61:32:14	20th Dec 2010	41

(LTE), has been described in detail by Ho & Townes (1983) and applied to observational data by numerous authors (e.g. Rosolowsky et al. 2008; Friesen et al. 2009; Morgan et al. 2010). The exact processes used here are described in detail by Morgan et al. (2013). We fit the hyperfine structure of the ammonia (1,1) and (2,2) lines using our own developed IDL[5] routines in conjunction with the IDL astronomy library routines (Landsman 1993). The results of the fitting allowed us to produce maps of kinetic and excitation temperature, linewidth, optical depth and column density. It should be noted here that our deduction of ammonia column density makes use of the assumption of LTE, i.e. that the excitation temperature (T_{ex}) of a source is equivalent to its kinetic temperature (T_k). The fact that derived values of T_{ex} are *not* approximately equal to values of T_k reflects the fact that T_{ex} is highly dependent upon the filling factor of the source in question as it is derived from a single transition. This has ramifications for observations of clumps which may be expected to form multiple cores as well as when making comparisons of regions which might be expected to be structurally different (i.e. filaments versus cores). This effect is particularly relevant to a study such as this one; the distances to Perseus and W3 are 260 pc and 2 kpc, respectively, leading to a significant difference in the physical scale which is being sampled in our observations. The filling factor of each source has been calculated from the assumption of LTE (see Morgan et al. 2010).

There are few ammonia observations of the W3 region on the scale of our coverage, though there are several of the area around W3(OH) (Wilson, Gaume & Johnston 1993; Zeng et al. 1984) as well as more complete coverage of W3 Main by Tieftrunk et al. (1998). Rosolowsky et al. (2008) performed a single-pointing survey of ammonia towards selected positions in the Perseus molecular cloud. A comparison of the derived physical parameters found by those authors, at positions for which we have matching data, shows consistency between the measurements at a level reflecting measurement errors of 10–20 per cent (see Section 4).

3 RESULTS

Figs 1 and 2 show the submillimetre maps of Hatchell et al. (2005) and Moore et al. (2007) covering the Perseus and W3 star-forming regions, respectively. Overlaid on the images are circles depicting the coverage of the GBT-KFPA ammonia maps presented here. Individual NH$_3$ (1,1) integrated intensity images are presented in Fig. 3. Noise values vary slightly between the Perseus and W3 regions, reflecting the lower integration times for some of our Perseus data. Individual rms values are presented with each map, but the Perseus data have rms off-source integrated intensity values in the range 0.36–0.86 K km s^{-1} with a mean of 0.49 K km s^{-1}. For W3 the range is 0.18–0.47 K km s^{-1} with a mean of 0.28 K km s^{-1}. As mentioned in Section 2, there is a radial variation in rms in our maps outside of a 3.5 arcmin radius, due to the inconsistent sampling of the 'daisy' pattern observing mode. This radial variation in noise due to the inconsistent sampling of the 'daisy' pattern observing mode is particularly obvious in Perseus map 11.
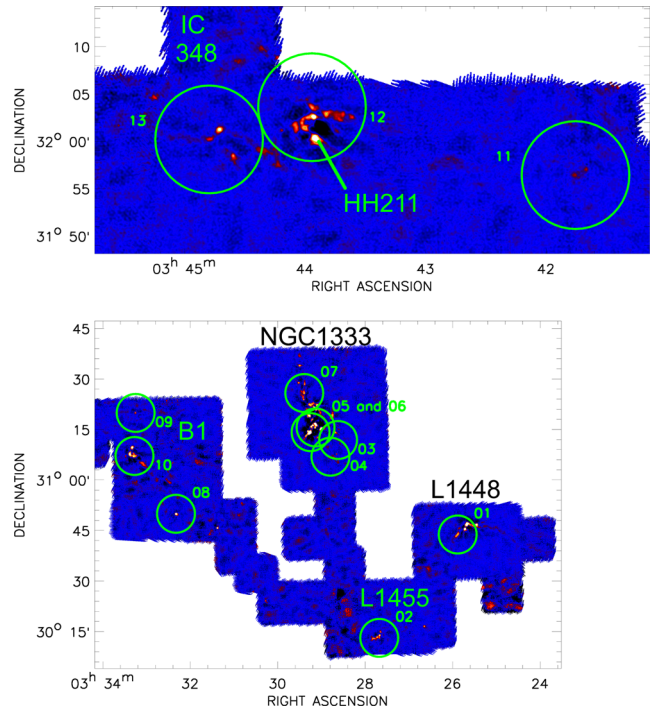

Figure 1. Extracts from the 850 µm submillimetre SCUBA map of the Persus region from Hatchell et al. (2005) overlaid with circles showing the coverage of each observed NH$_3$ inversion line map, including the undersampled regions outside of a ∼3.5 arcmin radius. The eastern portion of the Perseus molecular cloud complex is shown in the top panel with the western portion shown in the bottom panel. Some well-known regions are labelled.
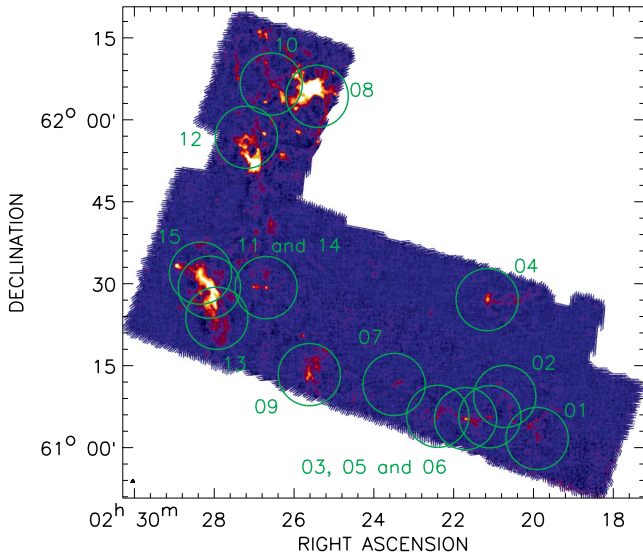
Figure 2. The 850 μm submillimetre SCUBA map of the W3 region from Moore et al. (2007) overlaid with circles showing the coverage of each observed NH_3 inversion line map, including the under-sampled regions outside of a ∼3.5 arcmin radius.

The ammonia maps sample the majority of the Perseus and W3 regions associated with submillimetre emission. Although the sampling can be seen to be less than complete, the brightest, most extended sources in the submillimetre are covered by our observations. Our observations of Perseus cover at least some portion of each of the well-known regions identified as B5, IC348, B1, NGC1333, L1455 and L1448. The High Density Layer (HDL) identified by Lada et al. (1978) on the eastern edge of the W3 GMC is covered approximately equally with the more diffuse material in the southwest portion of the cloud. The W3 ammonia maps cover 1178 arcmin^2 split approximately equally (51–49 per cent) between the HDL and the more diffuse region. Despite the equivalence in area between the two regions, more sources are found in the HDL. Our maps cover 192 of the submillimetre sources from the catalogue of Moore et al. (2007), of these, 127 are within the HDL and 65 are to the southwest of the W3 region.

The integrated intensity maps presented in Fig. 3 show a mixture of condensed cores (e.g. Perseus Map 08) and extended structure (e.g. W3 Map 13) with multiple examples of apparent filamentary morphology (e.g. Perseus Map 06, W3 Map 14). A large proportion show multiple cores contained within apparently connected extended structures (e.g. Perseus Map 12).

3.1 Source extraction

In order to locate individual NH_3 sources, the Starlink-CUPID[6] implementation of the CLUMPFIND (Williams, de Geus & Blitz 1994) package was run on integrated emission maps produced from the reduced spectral cubes. The reasons for running the two-dimensional implementation of CLUMPFIND rather than a full three-dimensional analysis on our spectral cubes are two-fold; first, some results show that the three-dimensional implementation of CLUMPFIND may underestimate the mass of clumps in star formation regions (Smith, Clark & Bonnell 2008) and is not as robust as the two-dimensional version (Pineda, Rosolowsky & Goodman 2009), particularly in

[6] http://docs.jach.hawaii.edu/star/sun255.htx/sun255.html

cases of limiting resolution [cf. Ward et al. (2012), who find that the three-dimensional extraction is the most accurate implementation when recovering simulated clumps]. Secondly, we found that no clump velocity separations exceeded the maximum linewidth found in the relevant map from which the clumps were extracted. Thus, the separations of any multiple spectral components along the line of sight are smaller than or approximately equal to typical clump linewidths and so the need for a three-dimensional extraction is somewhat negligible. Rosolowsky et al. (2008) performed a single-pointing survey of suspected cores in Perseus. Of the 193 sources in their catalogue, only six showed unambiguous evidence of multiple components with a mean velocity separation of 0.63 km s^{-1}. The mean observed linewidth of sources in our sample of Perseus cores is 0.64 km s^{-1} (see Table 6) and so we are unlikely to be able to separate any multiple components in this region, though they are likely present.

CLUMPFIND was run using a lowest contour level of three times the rms off-source noise (σ) measurements within the completely sampled portion of each individual map and successive contours spaced by 1σ. The minimum pixel count required to define a source was left at the default 7 (6 arcsec) pixels, although preliminary tests showed that results were insensitive to an increase in this parameter to 20 pixels, the size of the beam. Where individual maps overlap, sources in the overlap region were extracted from the mosaicked image rather than the individual Daisy scans. Each extracted source was examined in order to identify and discard any sources unduly affected by the higher noise values at the edges of our maps.

3.2 Source properties

With the above search parameters, CLUMPFIND detected 84 discrete ammonia sources in Perseus and 54 in W3. Applying the masks produced by CLUMPFIND to the parameter maps which resulted from our fitting analysis routines (Section 2.2) allows us to extract the distribution of column density, kinetic temperature, etc. for each detected core. In this paper we present the integrated properties of these extracted cores and leave analysis of any spatial variation of these parameters within the cores for subsequent publications. The central positions of each source, measured integrated intensities, fitted linewidths LSR velocities and any relevant matches from the point source catalogue of Rosolowsky et al. (2008) are presented in Tables 2 and 3. Where a source position listed in the catalogues of either Hatchell et al. (2005) or Moore et al. (2007) is within the lowest contour of the ammonia emission as extracted by CLUMPFIND in this work, we have also listed that association.

Derived physical properties, integrated over the NH_3 source extent, are presented in Tables 4 and 5. Turbulent velocity dispersions of each source were estimated by deconvolving the thermal contributions to the observed linewidths, $dV_{therm} = \sqrt{8k_B T_k \ln 2/m_{NH_3}}$, where T_k is the mean kinetic temperature averaged over the source in question and m_{NH_3} is the molecular mass of an ammonia molecule (17.03 amu). A statistical summary of the NH_3 source properties is given in Table 6 and their distributions are presented in Fig. 4. The properties of the Perseus and W3 samples appear distinct and this is confirmed by Kolmogorov–Smirnov (KS) tests indicating that the physical parameters of the Perseus and W3 samples represent distinct populations with confidence levels of 5σ, except for column density, which is distinct with a confidence level of 4σ.

Despite the significant extent of ammonia emission which is seen in the majority of our sources, it should be noted that filling
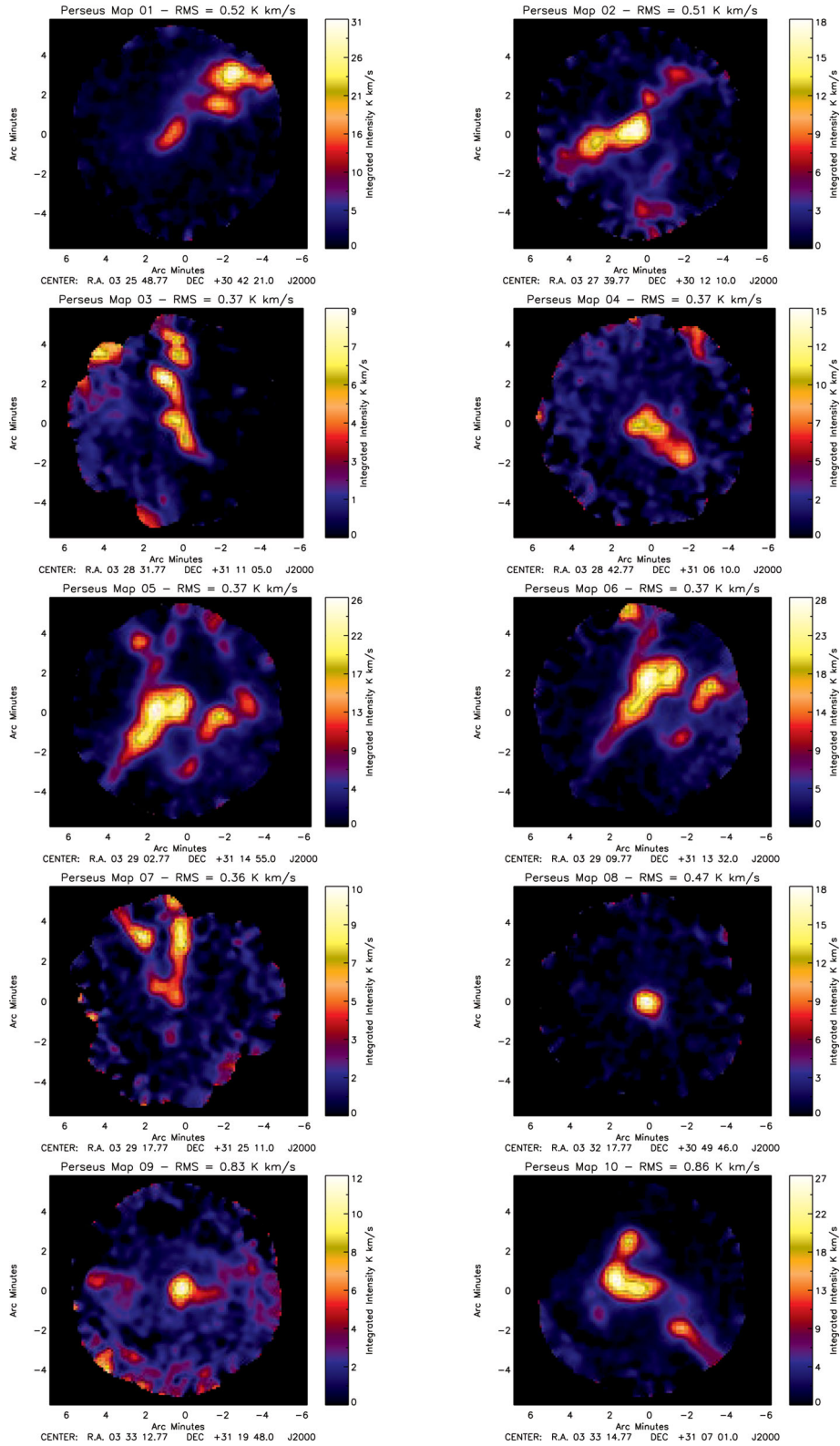
Figure 3. The Perseus and W3 integrated intensity maps.

factors considerably lower than unity are the norm across both the W3 and Perseus regions, with mean values of 0.12 and 0.42, respectively. This likely indicates a significant level of unresolved structure in the objects which we are observing. As noted in Section

2.2, we have made the assumption in our analysis that the gas we are observing is in LTE (i.e. that $T_{\mathrm{ex}} = T_{\mathrm{k}}$). This has the consequence that filling factors are essentially incorporated into our calculation of the source-averaged column density.

Figure 3 – *continued*
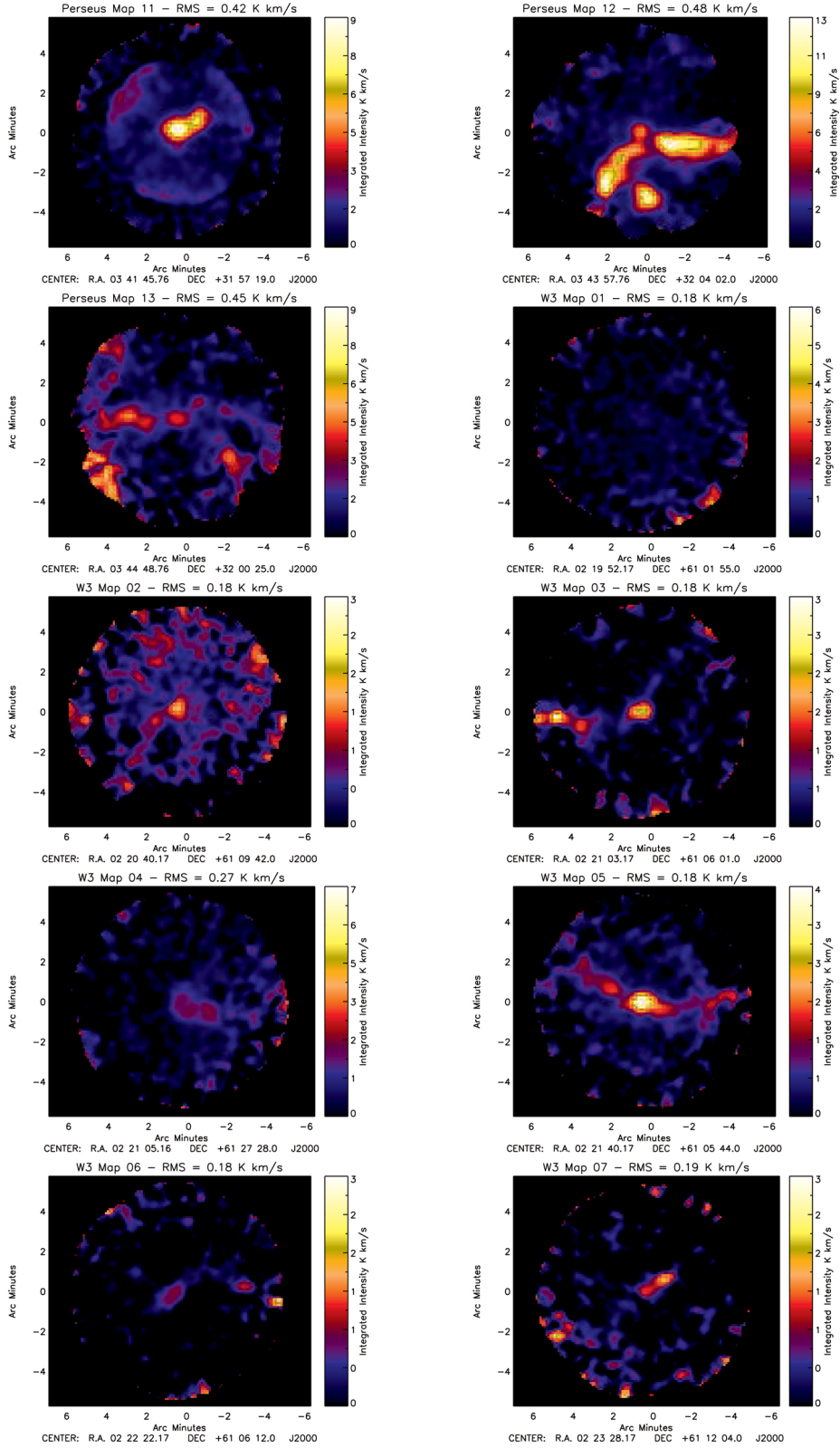
In general, the Perseus sources have smaller linewidths and turbulent velocity dispersions (σ_{turb}), higher optical depths and filling factors than those in W3. These results might be expected for any two given star-forming regions at the relative distances of W3 and

Perseus. The observations of Perseus map a physical scale a factor of 7.7 smaller than those of W3, assuming distances to Perseus and W3 of 260 pc and 2 kpc, respectively, and it is to be expected that there will be systematic resolution effects upon the measured core
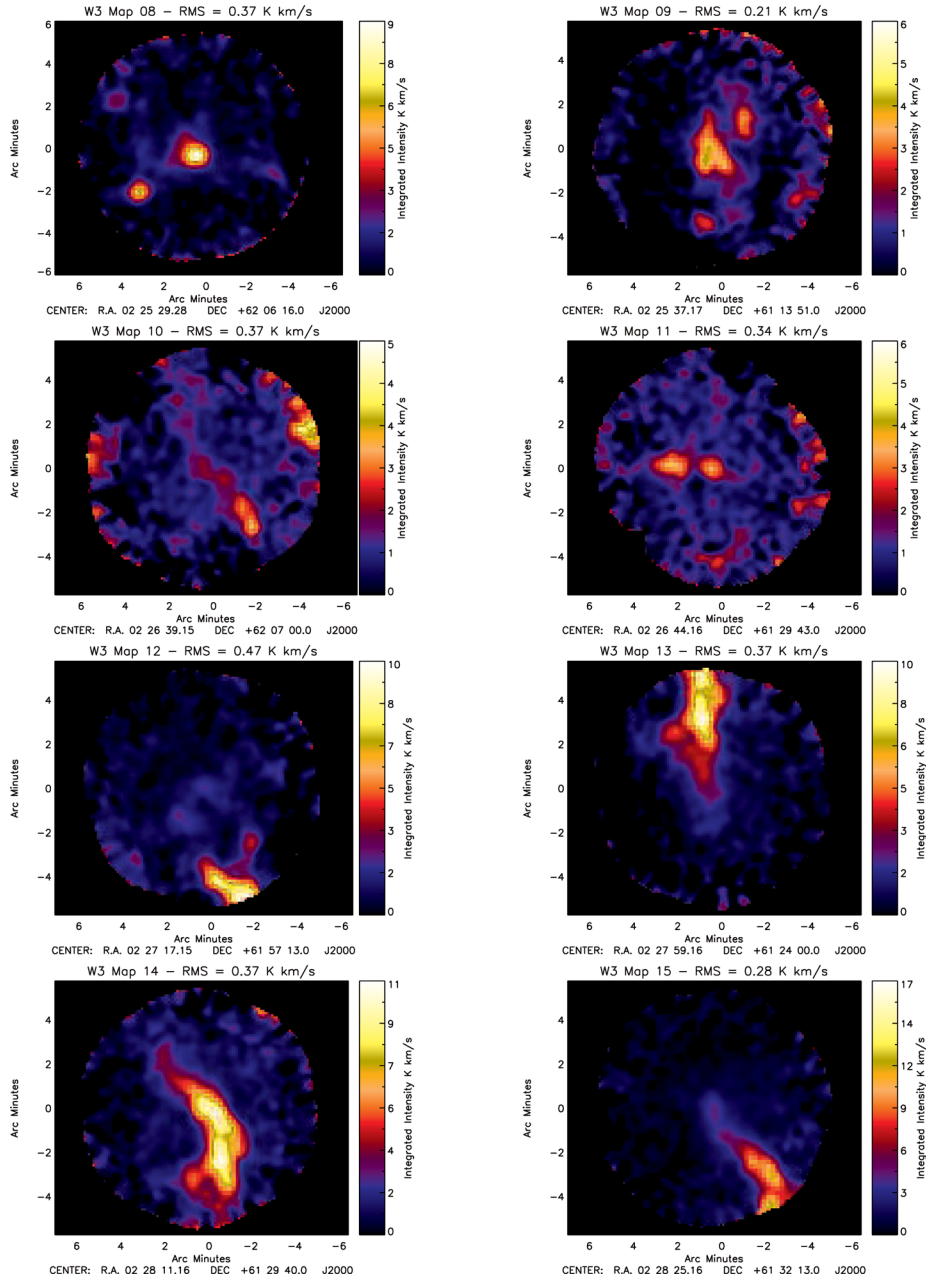
Figure 3 – *continued*

properties. For instance, filling factors may be expected to be lower in more distant sources where there is unresolved structure, while linewidths may be larger due to the inclusion of larger physical scales and blending of multiple sources.

3.3 Source associations

In the Perseus region, 60 protostars or prestellar cores from the catalogue of Hatchell et al. (2007) are covered by our NH$_3$ observations and all are associated with (1,1) line emission. These are evenly split between individual matches and multiple associations, with 30 submillimetre sources matched one-to-one with a single ammonia clump. A total of 11 ammonia clumps cover the remaining 30 submillimetre sources. There are no cases of a single submillimetre source being associated with more than one ammonia clump

in Perseus. We find 43 ammonia clumps that do not have an associated submillimetre source in the catalogue of Hatchell et al. (2007). 12 of these are weakly detected and have no (2,2) line detection. Inspection of the position of the remaining detections in the original maps of Hatchell et al. (2005) shows that weak submillimetre emission is often present below the detection limits used in the Hatchell et al. (2007) catalogue. In a few cases there is no apparent submillimetre emission whatsoever, although these are invariably near negative 'bowling' associated with nearby bright sources due to the observing method and Fourier-transform-based techniques used in the image reconstruction.

The ammonia maps of the W3 region cover the positions of 192 of the 316 submillimetre sources in the catalogue of Moore et al. (2007), 77 of which are detected in the (1,1) line. Compared to Perseus, there is a higher proportion of multiple associations

Table 2. Central positions and matching sources for each mapped source in Perseus.

Source	Central position RA (J2000)	Dec. (J2000)	W(NH₃(1,1)) (K km s⁻¹)	dV (km s⁻¹)	V_{LSR} (km s⁻¹)	Matching submm source[a]	Matching source (Rosolowsky et al. 2008)
P01	03:25:29.5	30:44:47	7.92 ± 0.52	0.78	4.11	31	
P02	03:25:36.9	30:45:23	2.95 ± 0.52	0.73	4.32	27, 28	R10, R12
P03	03:25:39.8	30:43:53	7.82 ± 0.52	0.75	4.73	29, Bolo11	R15, R14
P04	03:25:48.1	30:45:25	2.47 ± 0.52	0.61	4.45		
P05	03:25:50.3	30:42:32	6.00 ± 0.52	0.59	4.28	32	R17, R18, R19
P06	03:25:55.7	30:41:02	1.86 ± 0.52	0.81	3.99		R20
P07	03:26:00.3	30:42:07	2.12 ± 0.52	0.95	4.21		
P08	03:26:00.6	30:40:51	1.85 ± 0.52	–	–		
P09	03:27:31.0	30:15:09	4.42 ± 0.51	0.42	4.87		R29
P10	03:27:35.0	30:10:22	2.68 ± 0.51	0.52	5.02		R30
P11	03:27:36.5	30:13:58	3.84 ± 0.51	0.81	4.55	39	R31
P12	03:27:37.8	30:08:37	3.95 ± 0.51	0.53	5.28		
P13	03:27:41.3	30:12:17	8.31 ± 0.51	0.70	4.79	35, 36, 40	R32, R33, R34
P14	03:27:45.7	30:08:39	2.21 ± 0.51	0.73	5.30		
P15	03:27:49.7	30:11:40	6.07 ± 0.51	0.66	4.82	37	R35
P16	03:27:54.6	30:09:46	2.45 ± 0.51	0.65	4.60		
P17	03:27:56.6	30:11:15	4.47 ± 0.51	0.51	4.89		
P18	03:27:56.8	30:10:24	3.90 ± 0.51	0.60	4.64		
P19	03:28:28.6	31:10:07	2.85 ± 0.37	0.34	6.98		
P20	03:28:30.7	31:15:14	3.15 ± 0.37	0.40	7.40		
P21	03:28:31.8	31:11:26	3.34 ± 0.37	0.42	7.02	74	R40
P22	03:28:33.7	31:13:12	3.71 ± 0.37	0.47	7.13	49	R44
P23	03:28:33.8	31:04:39	3.67 ± 0.37	0.46	6.57	Bolo26	R41
P24	03:28:35.0	31:06:47	1.80 ± 0.37	0.44	6.67	69	R43
P25	03:28:39.5	31:05:50	5.40 ± 0.37	0.49	6.87	71	R46
P26	03:28:44.3	31:06:10	4.18 ± 0.37	0.59	7.11	75	R50
P27	03:28:49.9	31:12:50	2.32 ± 0.37	1.28	7.16		
P28	03:28:52.6	31:14:51	7.21 ± 0.37	1.04	7.54	44	R58
P29	03:28:56.5	31:13:57	6.07 ± 0.37	0.83	6.98		
P30	03:29:01.7	31:12:23	4.48 ± 0.37	0.72	6.95	65	R65
P31	03:29:02.6	31:15:26	9.58 ± 0.37	1.22	7.53	43, 52	R67, R68
P32	03:29:08.3	31:17:22	4.95 ± 0.37	0.72	8.16	46, 62, Bolo44	R72
P33	03:29:09.0	31:15:21	2.05 ± 0.37	1.02	7.63	50, 51	R70, R73
P34	03:29:13.4	31:13:20	6.32 ± 0.37	0.98	7.35	41, 42, 48, 59, 72	R75, R78, R80, R83
P35	03:29:17.1	31:28:15	4.49 ± 0.36	0.40	7.34	61	R81
P36	03:29:17.7	31:25:51	3.01 ± 0.36	0.55	7.11	57	R82
P37	03:29:19.5	31:23:36	1.97 ± 0.36	0.59	7.35	63, 67	R84
P38	03:29:20.9	31:29:22	2.10 ± 0.36	–	–		
P39	03:29:22.6	31:26:11	2.72 ± 0.36	0.35	7.17		
P40	03:29:26.0	31:28:14	3.53 ± 0.36	0.40	7.30	64	R88
P41	03:32:16.1	30:49:38	5.52 ± 0.47	0.55	6.63	76	R103
P42	03:32:55.3	31:21:02	3.10 ± 0.83	0.72	6.34		
P43	03:32:57.8	31:04:10	5.79 ± 0.86	0.40	6.42		
P44	03:32:58.6	31:20:43	2.90 ± 0.83	0.70	6.37		R112
P45	03:32:59.9	31:03:36	6.10 ± 0.86	0.40	6.45		
P46	03:33:02.2	31:20:13	2.84 ± 0.83	0.77	6.44		
P47	03:33:04.7	31:05:01	6.93 ± 0.86	0.50	6.41	5	R113, R114
P48	03:33:05.7	31:06:28	4.32 ± 0.86	0.48	6.32		R115
P49	03:33:10.5	31:19:47	5.17 ± 0.83	0.50	6.62	82	R118
P50	03:33:14.5	31:07:12	0.28 ± 0.86	0.64	6.24	4, 7	R119
P51	03:33:17.4	31:09:20	7.72 ± 0.86	0.72	6.21	1	R121
P52	03:33:21.0	31:07:37	3.54 ± 0.86	0.74	6.45	2	R123
P53	03:33:24.3	31:05:55	4.58 ± 0.86	0.48	6.59		R124
P54	03:33:25.0	31:19:51	2.95 ± 0.83	0.89	6.29		R125
P55	03:33:26.3	31:06:59	3.95 ± 0.86	0.69	6.61	10	R126
P56	03:33:31.0	31:20:22	3.58 ± 0.83	0.82	6.30		R127
P57	03:41:29.8	31:57:42	1.83 ± 0.42	–	–		
P58	03:41:32.9	31:59:09	1.61 ± 0.42	–	–		
P59	03:41:33.5	31:58:05	1.48 ± 0.42	–	–		
P60	03:41:36.4	31:54:41	1.48 ± 0.42	–	–		
P61	03:41:36.5	32:00:07	1.54 ± 0.42	–	–		
P62	03:41:41.1	31:57:58	3.64 ± 0.42	0.32	9.23	Bolo92	R145
P63	03:41:46.8	31:57:24	3.62 ± 0.42	0.42	9.24	Bolo94	R147

Table 2 – *continued*

| Source | Central position | | W(NH$_3$(1,1)) | dV | V_{LSR} | Matching submm | Matching source |
	RA(J2000)	Dec. (J2000)	(K km s^{-1})	(km s^{-1})	(km s^{-1})	Source^a	(Rosolowsky et al. [2008])
P64	03:41:48.0	31:54:20	1.76 ± 0.42	–	–		
P65	03:41:53.2	32:00:25	1.89 ± 0.42	–	–		
P66	03:41:53.4	31:54:33	1.68 ± 0.42	–	–		
P67	03:41:55.3	31:59:24	1.94 ± 0.42	0.42	9.20		
P68	03:41:58.8	31:58:54	2.36 ± 0.42	0.54	9.13		R148
P69	03:42:00.4	31:57:47	1.73 ± 0.42	0.61	9.07		
P70	03:43:39.4	32:03:10	4.09 ± 0.48	0.80	8.50	23	R156
P71	03:43:48.0	32:03:18	5.50 ± 0.48	0.62	8.49	15, 24, 26	R157, 158, 159, 160
P72	03:43:55.9	32:00:45	4.24 ± 0.48	0.78	8.69	12	R161
P73	03:43:57.3	32:04:03	3.76 ± 0.48	0.75	8.26	17	R163
P74	03:44:01.0	32:02:43	5.02 ± 0.48	0.62	8.47	13, 16, 18, 21	R162, 164, 165
P75	03:44:05.3	32:01:34	5.73 ± 0.48	0.62	8.40	20	R169
P76	03:44:31.0	32:00:35	1.68 ± 0.45	0.66	9.00		
P77	03:44:36.9	32:00:59	2.00 ± 0.45	0.53	9.11		
P78	03:44:37.4	31:58:42	3.00 ± 0.45	0.68	9.71	19	R176
P79	03:44:39.8	31:59:36	1.73 ± 0.45	0.90	9.55		
P80	03:44:44.1	32:01:17	2.03 ± 0.45	1.08	9.57	14	R178
P81	03:44:49.4	32:00:40	2.45 ± 0.45	0.50	8.79	25	R180
P82	03:44:56.1	32:00:25	2.35 ± 0.45	0.53	8.88		R181
P83	03:45:01.1	32:00:42	2.95 ± 0.45	0.40	8.93		
P84	03:45:06.3	32:00:35	2.70 ± 0.45	0.54	8.93		

^{a}Sources taken from Hatchell et al. ([2007]), incorporating several Bolocam sources from Enoch et al. ([2006]) labelled as 'Boloxx'.

with 25 one-to-one matches and 52 submillimetre sources that are matched with 17 NH$_3$ clumps. 12 ammonia clumps were found that were not detected in the catalogue of Moore et al. ([2007]). Of these, eight are weak with no (2,2) detection and two are close to the edge of a submillimetre map. The remaining two (W26 and W47) are near to bright submillimetre sources [objects 109 and 213 in the catalogue of Moore et al. ([2007]), respectively] and may be associated with these. However, these submillimetre sources are more strongly associated (closer, with more morphological similarity) to two other ammonia clumps (W23 and W46). There is clear separation of the ammonia clump pairs in each case and so these sources have not been amalgamated. There is a single case in our entire set of observations in which two ammonia clumps appear to be clearly associated with a single submillimetre source. The sources W35 and W38 are both associated with the source 175 from the catalogue of Moore et al. ([2007]).

In Section 2 it was stated that the coverage of sources in both the Perseus and W3 regions was selected to include both clustered and isolated sources, with some bias towards clustered regions. In order to test for selection effects that may affect our results, we have plotted the distributions of integrated submillimetre flux densities for both regions in Fig. [5]. It can be seen that a high proportion of sources with low flux densities fall outside our NH$_3$ observations, but that the populations are virtually fully sampled down to the primary turnovers in both distributions, where the original submillimetre catalogues become incomplete. Also, the proportion of submillimetre sources covered is very similar (as a function of flux density) in Perseus and W3. We therefore find no significant difference in the selection of the two samples which might result in artificial differences between them.

A comparison between the integrated submillimetre flux densities of sources detected (red) and not-detected (blue) in ammonia in W3 is shown in Fig. [6] (no corresponding plot is presented for Perseus as all observed submillimetre sources within that region were detected). The figure shows that, as expected, it is generally the sources that are weaker in submillimetre continuum which are not

detected by this survey. However, there is considerable overlap and so the likelihood of detecting a submillimetre source in ammonia is not completely determined by the NH$_3$ detection limit.

In Fig. [7] we plot the integrated 850 μm flux density of each source against the integrated NH$_3$ (1,1) line intensity of the corresponding source. Significant correlations between the two measurements are seen, at >5 sigma levels of significance. The offset between the W3 and Perseus samples in this figure are produced by the higher average temperatures in the W3 sample (Table [6] and Fig. [4]) which produce higher continuum flux densities and lower NH$_3$ intensities for a given column density.

Fig. [8] shows the relationship between the column density derived from ammonia and the integrated intensity in the (1,1) line. Where a submillimetre association has been identified, the source is plotted as a circle whose diameter represents the 850 μm integrated flux density. Ammonia detection limits are marked by dashed lines, with small filled circles representing the limiting values of the submm emission, taken from Hatchell et al. ([2005]) and Moore et al. ([2007]). The lower limits for the detection of ammonia integrated intensity represent three times the median rms values in the integrated intensity images for the relevant region, the value used as the minimum threshold in the CLUMPFIND-based extractions. As there is no unique lower limit on column density measurements, the plotted limit is simply taken as the lowest measured value in the relevant region.

Lines of best fit have been added to Fig. [8] to emphasize the correlation of column density and integrated intensity for the separate W3 and Perseus samples resulting from the LTE analysis. The offset and slightly differing slopes for the two samples are again due to the higher average temperature of cores in W3 and the scatter results from variations in T_k within each sample. Where there is no associated submillimetre detection, the ammonia source is plotted as a star (W3) or diamond (Perseus). The plot shows that, at least for the Perseus sample, sources that are detected in ammonia with no 850 μm association have the lowest NH$_3$ integrated intensity and column density. There is considerable overlap between the

Table 3. Central positions and matching sources for each mapped source in W3.

Source	Central position RA (J2000)	Dec. (J2000)	$W(NH_3(1,1))$ (K km s^{-1})	dV (km s^{-1})	V_{LSR} (km s^{-1})	Matching submm source (Moore et al. 2007)
W01	02:20:34.9	61:26:43	1.26 ± 0.27	–	–	27
W02	02:20:39.9	61:09:59	0.82 ± 0.18	0.67	−48.93	29
W03	02:20:44.2	61:27:06	1.06 ± 0.27	1.03	−51.92	30
W04	02:20:44.6	61:25:58	1.02 ± 0.27	–	–	
W05	02:20:48.6	61:12:24	0.72 ± 0.18	–	–	
W06	02:20:53.1	61:26:58	1.56 ± 0.27	1.75	−51.05	31
W07	02:21:00.9	61:26:58	1.59 ± 0.27	1.43	−51.48	35
W08	02:21:04.4	61:27:41	1.38 ± 0.27	0.97	−51.17	38
W09	02:21:05.8	61:05:58	1.12 ± 0.18	0.78	−49.86	37
W10	02:21:35.8	61:05:33	1.30 ± 0.18	0.96	−49.97	39, 42, 43, 44, 45
W11	02:21:53.9	61:06:23	0.96 ± 0.18	1.20	−50.01	47, 49, 50
W12	02:22:03.4	61:07:18	0.66 ± 0.18	–	–	51
W13	02:22:24.7	61:06:04	0.70 ± 0.18	0.82	−49.99	54
W14	02:23:20.6	61:12:41	1.13 ± 0.19	0.58	−50.11	60
W15	02:23:27.2	61:12:11	0.96 ± 0.19	0.67	−50.11	61
W16	02:24:58.6	62:05:07	1.73 ± 0.37	0.97	−39.68	
W17	02:25:07.3	62:05:29	1.25 ± 0.37	1.05	−39.92	78
W18	02:25:25.7	61:15:05	1.63 ± 0.21	1.04	−48.86	85, 86, 91
W19	02:25:27.6	61:16:25	1.33 ± 0.21	–	–	87, 92, 98
W20	02:25:29.2	62:07:23	1.30 ± 0.37	–	–	
W21	02:25:29.7	61:11:01	1.10 ± 0.21	1.10	−48.73	90
W22	02:25:31.1	61:13:03	1.71 ± 0.21	1.18	−48.30	100, 95, 97
W23	02:25:32.2	62:06:03	3.12 ± 0.37	3.50	−42.84	109, 99
W24	02:25:40.4	61:10:29	1.50 ± 0.21	1.22	−47.92	
W25	02:25:40.7	61:13:55	2.02 ± 0.21	0.92	−47.83	103, 105, 107, 111, 112
W26	02:25:51.4	62:06:18	1.36 ± 0.37	2.08	−38.77	
W27	02:25:52.9	62:04:17	2.93 ± 0.37	1.75	−38.78	119
W28	02:26:02.2	62:08:43	1.97 ± 0.37	1.41	−38.42	127
W29	02:26:20.8	62:04:21	1.99 ± 0.37	2.06	−39.84	142
W30	02:26:26.3	62:05:18	1.77 ± 0.37	1.64	−39.38	148
W31	02:26:30.1	61:29:38	1.20 ± 0.34	0.85	−47.08	150
W32	02:26:33.3	61:26:48	1.42 ± 0.34	–	–	
W33	02:26:35.6	62:06:42	1.51 ± 0.37	1.42	−39.15	152, 161, 166
W34	02:26:37.3	61:25:46	1.55 ± 0.34	–	–	
W35	02:26:41.6	61:32:49	1.31 ± 0.34	0.94	−47.88	175
W36	02:26:42.1	61:25:23	1.77 ± 0.34	–	–	
W37	02:26:43.1	61:33:34	1.23 ± 0.34	–	–	171
W38	02:26:43.4	61:31:49	1.17 ± 0.34	1.11	−47.79	175
W39	02:26:44.2	61:29:48	1.80 ± 0.34	1.25	−47.69	172
W40	02:26:45.8	62:08:41	1.26 ± 0.37	1.41	−38.68	176, 180
W41	02:26:48.2	61:25:39	1.62 ± 0.34	–	–	
W42	02:26:49.8	62:10:04	1.40 ± 0.37	–	–	
W43	02:26:59.3	61:54:45	1.93 ± 0.47	0.80	−45.45	196
W44	02:26:59.6	61:29:51	2.03 ± 0.34	1.78	−47.69	195, 214
W45	02:26:60.0	61:53:50	1.68 ± 0.47	1.99	−45.17	198
W46	02:27:02.6	61:52:03	4.25 ± 0.47	2.78	−47.20	213
W47	02:27:11.2	61:53:05	3.24 ± 0.47	2.47	−48.48	
W48	02:28:01.8	61:24:34	2.29 ± 0.37	1.84	−48.05	262, 270, 275, 280, 281, 286
W49	02:28:01.9	61:27:22	5.22 ± 0.37	1.61	−48.63	266, 268, 284, 288
W50	02:28:05.3	61:29:58	4.49 ± 0.37	1.86	−47.85	264, 285, 287, 290, 292
W51	02:28:09.8	61:25:41	2.84 ± 0.37	2.11	−47.49	289, 293
W52	02:28:15.1	61:26:38	2.83 ± 0.37	2.46	−48.02	291
W53	02:28:23.1	61:31:52	2.19 ± 0.37	1.94	−47.04	297, 299, 300
W54	02:28:58.7	61:33:29	1.11 ± 0.19	0.81	−51.46	315

submillimetre associations and non-associations, but the overall trend of submillimetre associations representing sources with the highest NH$_3$ intensity and column density is clear.

Fig. 8 displays the differing sensitivity limits in what are effectively four observational samples. Our observations of the Perseus and W3 regions have different average sensitivity limits, while there is also a notable difference between the sensitivity of sub-

millimetre observations in W3 and Perseus. These differences explain the number of objects detected at 850 µm by Moore et al. (2007) which are not found in NH$_3$, while all objects detected at 850 µm by Hatchell et al. (2005) are seen in our observations. The relative completeness of these samples is limited by a combination of the limits of our ammonia observations and those of the relevant submillimetre observations. In particular, by

Table 4. Derived physical properties for each mapped source in Perseus.

Source	T_k (K)	Optical depth	Filling factor	Column density ($/10^{13}$ cm^{-2})	Source	T_k (K)	Optical depth	Filling factor	Column density ($/10^{13}$ cm^{-2})
P01	11.30	4.13	0.70	42.87	P43	10.40	4.54	0.54	27.49
P02	11.37	4.01	0.81	46.44	P44	14.09	0.82	0.51	11.06
P03	11.40	2.85	0.60	36.05	P45	10.01	4.36	0.61	27.05
P04	13.47	1.64	0.22	22.02	P46	12.55	1.48	0.28	20.63
P05	10.19	4.14	0.62	34.65	P47	10.30	4.57	0.60	32.43
P06	15.69	1.21	0.21	18.16	P48	10.82	2.66	0.48	19.73
P07	18.56	1.75	0.07	54.21	P49	10.14	5.15	0.42	33.99
P08	–	–	–	–	P50	11.63	4.50	0.62	44.07
P09	11.39	3.04	0.47	20.81	P51	12.22	2.70	0.53	34.22
P10	12.88	1.16	0.49	10.69	P52	11.18	4.44	0.72	52.61
P11	13.36	1.60	0.38	25.35	P53	10.52	3.99	0.45	26.56
P12	12.92	1.81	0.53	15.87	P54	12.38	1.76	0.25	28.44
P13	12.69	3.10	0.60	35.74	P55	12.41	1.54	0.48	19.14
P14	19.99	0.93	0.26	21.65	P56	12.88	1.96	0.26	33.21
P15	12.75	2.19	0.61	22.89	P57	–	–	–	–
P16	17.26	0.87	0.33	18.94	P58	–	–	–	–
P17	11.84	2.29	0.64	18.33	P59	–	–	–	–
P18	13.74	1.54	0.56	15.92	P60	–	–	–	–
P19	10.35	3.66	0.35	17.79	P61	–	–	–	–
P20	10.84	5.49	0.37	34.49	P62	9.45	4.78	0.42	22.59
P21	11.58	3.50	0.32	23.10	P63	10.49	3.35	0.39	22.87
P22	12.00	3.37	0.34	27.37	P64	–	–	–	–
P23	11.41	3.34	0.42	25.25	P65	–	–	–	–
P24	11.61	4.40	0.15	30.65	P66	–	–	–	–
P25	10.45	3.62	0.53	27.23	P67	14.33	1.97	0.11	15.37
P26	11.82	3.76	0.41	32.52	P68	14.52	1.00	0.25	8.50
P27	17.82	1.10	0.29	43.15	P69	15.39	1.31	0.24	9.59
P28	14.69	1.57	0.52	38.32	P70	16.52	1.32	0.36	23.58
P29	14.17	1.75	0.48	28.66	P71	13.49	2.28	0.48	22.87
P30	13.89	1.85	0.44	23.41	P72	16.38	1.99	0.32	34.25
P31	16.45	1.93	0.45	55.50	P73	15.18	1.71	0.29	25.46
P32	14.56	2.08	0.46	30.47	P74	13.25	2.27	0.44	23.89
P33	13.74	1.95	0.75	42.11	P75	12.16	2.66	0.47	31.10
P34	13.19	1.49	0.59	30.53	P76	16.88	0.78	0.21	10.81
P35	12.03	3.21	0.46	22.51	P77	13.59	1.02	0.30	10.76
P36	12.63	2.10	0.36	21.50	P78	13.23	1.55	0.35	19.04
P37	14.86	1.97	0.14	24.40	P79	18.86	0.53	0.20	15.41
P38	–	–	–	–	P80	15.37	0.61	0.24	17.85
P39	12.63	1.98	0.34	12.98	P81	12.62	1.90	0.28	17.64
P40	10.99	3.11	0.45	21.72	P82	12.13	1.21	0.43	9.32
P41	12.07	2.86	0.51	31.34	P83	11.76	2.17	0.42	14.60
P42	17.44	0.48	0.45	11.83	P84	13.21	2.66	0.22	24.50

submillimetre sensitivity in Perseus and by ammonia sensitivity in W3.

3.4 The relationship between submillimetre and ammonia emission

Fig. 9 shows the positional offsets between the peaks in ammonia integrated intensity and submillimetre continuum for each associated source. In the case of multiple submillimetre source associations, the closest peak is used. While the two tracers share common regions of emission, the peaks may be separated by some distance. The surface density distributions of peak offsets are plotted in Fig. 10. While there are some sources with offsets consistent with the pointing errors (∼4 arcsec), there is a significant excess with much larger separations and approximately 40 per cent are larger than the radius of the GBT beam. In addition, we see a minimum in the Perseus distribution at zero offset. These results show that the locations of the emission peaks in the submillimetre continuum are not tightly constrained to those in ammonia.

The relative distribution of the two tracers is shown in Fig. 11 for six representative sources (P05, P33 & P41 and W18, W25 & W49), with submillimetre continuum contours overlaid upon NH$_3$ (1,1) line intensity images. A single white, broken contour is overlaid on the images which traces the NH$_3$ column density distribution at a level representative of the source shape and size (this is the 50 per cent contour unless explicitly stated otherwise). In the Perseus sources, the ammonia emission is typically significantly more extended than the continuum while in the W3 sources there is less of a disparity. P33 and all the W3 images in Fig. 11 show multiple submillimetre cores within the 50 per cent ammonia emission contour. Equivalent images for all associated sources are presented in online material.

It has been noted by previous authors (see Reid et al. 2010 and references therein, also Curtis & Richer 2010) that different source-extraction techniques may produce significantly different results.

Table 5. Derived physical properties for each mapped source in W3.

Source	T_k (K)	Optical depth	Filling factor	Column density ($/10^{13}$ cm^{-2})	Source	T_k (K)	Optical depth	Filling factor	Column density ($/10^{13}$ cm^{-2})
W01	–	–	–	–	W28	21.88	0.92	0.11	46.84
W02	15.08	2.70	0.04	41.00	W29	22.83	0.85	0.10	67.41
W03	18.20	1.65	0.03	71.82	W30	20.74	0.79	0.10	45.06
W04	–	–	–	–	W31	15.10	2.59	0.05	47.99
W05	–	–	–	–	W32	–	–	–	–
W06	17.71	1.56	0.06	84.70	W33	23.11	0.49	0.11	27.09
W07	15.83	1.02	0.12	33.69	W34	–	–	–	–
W08	15.41	1.29	0.10	32.16	W35	16.81	0.94	0.19	21.75
W09	13.49	1.42	0.11	23.40	W36	–	–	–	–
W10	14.64	1.29	0.14	25.19	W37	–	–	–	–
W11	16.12	1.11	0.08	31.36	W38	18.19	0.43	0.16	12.29
W12	–	–	–	–	W39	15.11	1.05	0.14	28.84
W13	17.40	0.60	0.13	14.07	W40	20.90	0.40	0.10	20.04
W14	12.44	3.48	0.08	39.87	W41	–	–	–	–
W15	15.10	3.23	0.05	37.49	W42	–	–	–	–
W16	16.91	1.71	0.11	43.33	W43	17.22	2.26	0.10	43.35
W17	17.24	1.18	0.09	31.82	W44	15.76	1.10	0.14	40.11
W18	13.75	1.32	0.18	27.68	W45	18.90	0.30	0.21	18.57
W19	–	–	–	–	W46	25.84	1.39	0.09	189.02
W20	–	–	–	–	W47	22.12	1.37	0.09	134.67
W21	17.60	0.67	0.13	19.53	W48	17.47	0.94	0.14	46.81
W22	13.88	1.61	0.14	35.70	W49	16.57	1.27	0.23	50.05
W23	35.04	0.73	0.08	199.64	W50	17.97	1.13	0.19	56.89
W24	15.66	0.70	0.20	19.31	W51	17.43	1.05	0.14	64.44
W25	12.54	1.98	0.17	35.18	W52	19.05	1.13	0.10	84.35
W26	34.73	0.32	0.08	48.97	W53	19.67	0.78	0.11	54.48
W27	21.67	1.10	0.11	71.82	W54	23.76	1.18	0.10	35.21

Table 6. Summary of physical properties for sources in Perseus and W3.

	Perseus			W3		
	Mean	Median	Std. dev.	Mean	Median	Std. dev.
dV (km s^{-1})	0.64	0.61	0.20	1.44	1.25	0.63
σ_{turb} (km s^{-1})	0.25	0.24	0.10	0.59	0.54	0.27
T_k (K)	13.14	12.69	2.31	18.50	17.43	4.85
Optical depth	2.42	2.08	1.24	1.27	1.13	0.72
Filling factor	0.42	0.43	0.16	0.12	0.11	0.05
Column density ($/10^{13}$ cm^{-2})	25.78	23.89	10.69	50.07	40.11	39.92

It may therefore be important to state that all sources identified here, in both ammonia and submillimetre emission, have been identified using CLUMPFIND. The size of each source was defined by its 50 per cent surface-brightness contour. Following Hatchell et al. (2007) we define R_{eff}, the effective radius of a source, as $\sqrt{(\frac{A}{\pi})}$, where A is the area within the 50 per cent contour, after deconvolving the beam assuming both a Gaussian source and beam. This deconvolution is only approximate as the assumption of a Gaussian source is somewhat unrealistic. R_{eff} values for all ammonia sources are presented in Tables 7 and 8, along with the sizes of the associated submillimetre sources, estimated in the same way. Histograms of the source–size distributions, comparing the two tracers and the two cloud samples, are shown in Fig. 12. Where the emission of an ammonia clump covers more than one submillimetre source, the combined area of all associations is used to calculate R_{eff} values. Ammonia sizes vary surprisingly little within and between the two regions, with mean deconvolved R_{eff} measurements of 35.6 arcsec and 32.6 arcsec for the Perseus and W3 samples, respectively. Despite the similarity in angular size between the regions, at the as-

sumed distances of Perseus and W3 (260 pc and 2 kpc, respectively) these correspond to physical radii of 0.05 and 0.31 pc. This large difference in physical scale seen here is discussed in more detail in Section 4.1.

Median angular sizes ($\widetilde{R_{eff}}$) agree with the means ($\overline{R_{eff}}$) to significantly better than the sample standard deviation in both cases, indicating that each sample is reasonably symmetrical ($\frac{\overline{R_{eff}} - \widetilde{R_{eff}}}{\sigma} = 0.33$ and 0.05 for Perseus and W3, respectively). The submillimetre and NH$_3$ sizes in W3 are distributed rather similarly whereas, in Perseus, submillimetre radii are significantly smaller, with barely any overlap between the histograms of the two tracers. KS tests of the submillimetre/ammonia R_{eff} ratios suggest that the populations of W3 and Perseus are significantly different in terms of relative source size. The probability that the distributions are drawn from the same population is measured at 2.3×10^{-7}.

To test for the effects of distance upon the derived source sizes, we convolved and regridded the Perseus maps (both ammonia and submillimetre) to an equivalent beam and pixel size to place it, effectively, at the distance of W3 (2 kpc) and then re-ran the
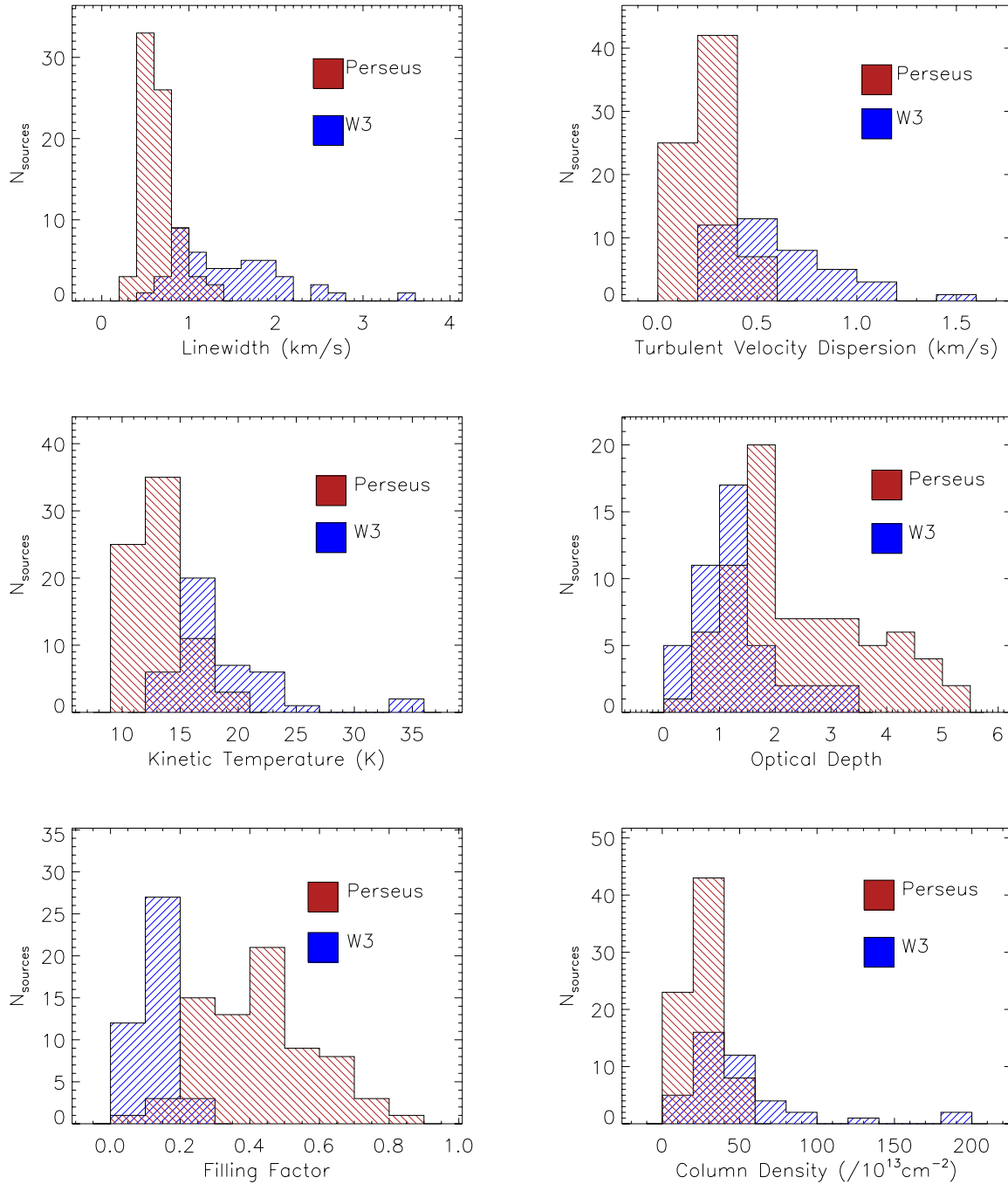
Figure 4. Histograms of the physical properties of the Perseus (red) and W3 (blue) regions.

source-extraction routines and subsequent analyses. In the majority of our KFPA 'daisy' maps this smoothing results in only a single source per map. We are thus limited in our analysis by our observing strategy of multiple isolated maps, rather than one, large-scale map. The source sizes found in the smoothed, regridded Perseus maps are shown in Table 9. It can be seen that the effect of artificially placing the Perseus sources at the distance of W3 decreases the measured size of sources in both submillimetre and ammonia emission by a factor of ∼2.

For a fixed beam size, sources with an intensity profile described by a power law will have a size dependent upon the index of that

power law (Young et al. 2003). Therefore, the fact that the ammonia source sizes in both Perseus and W3 are so similar may indicate that similar structures, with power-law intensity profiles, are being traced in each region. For example, large clumps/clouds of ammonia which envelop protostellar condensations. However, this scenario is contradicted in two ways. First, the source sizes measured in our smoothed Perseus maps are significantly smaller than those measured in the native resolution maps, indicative of a Gaussian or solid disc intensity profile (Enoch et al. 2007). Secondly, we see significant differences between the sizes of submillimetre sources in W3 and Perseus, inconsistent with the conclusion that sources
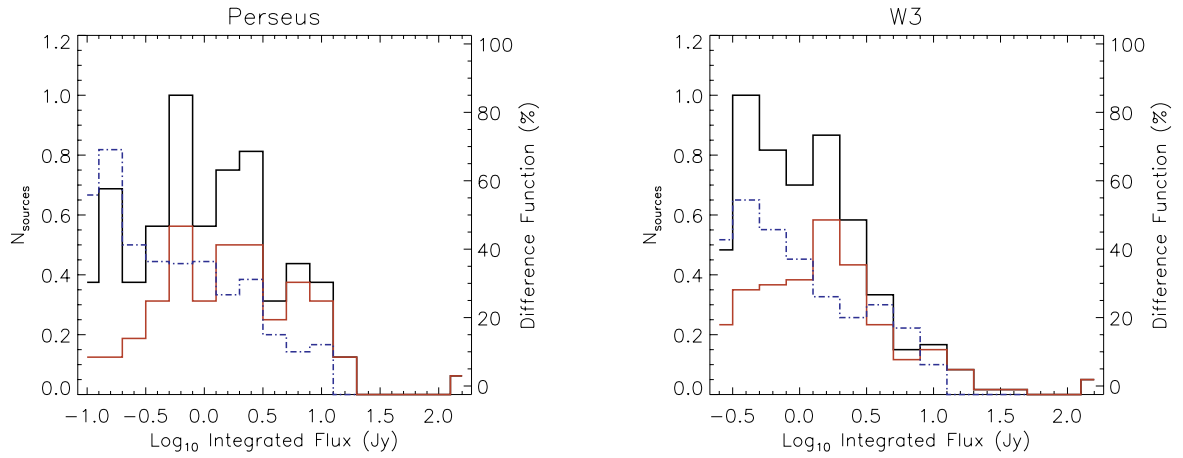
Figure 5. Distributions of the submillimetre integrated fluxes of the Perseus (left) and W3 (right). The solid black line shows the distribution of fluxes from the entire catalogue of either Hatchell et al. (2007) for Perseus or Moore et al. (2007) for W3. The solid red line shows the distribution of fluxes of those sources which are covered by our observations and the dashed blue line shows the difference between the two distributions.
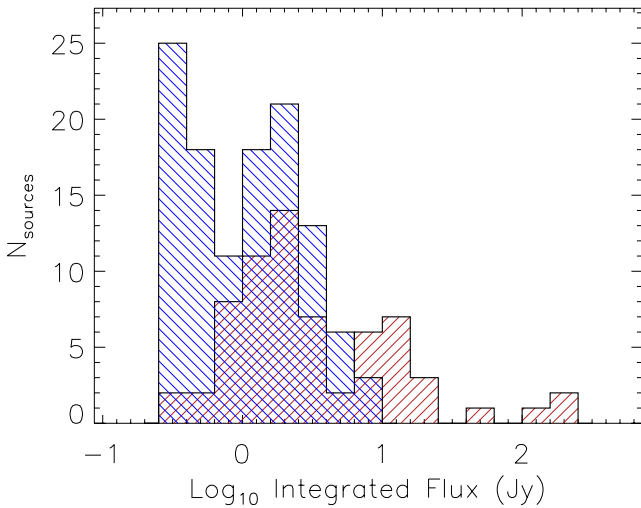
Figure 6. Histograms of the (log) integrated fluxes of the sources detected (red) and not-detected (blue) in the W3 region by this survey.
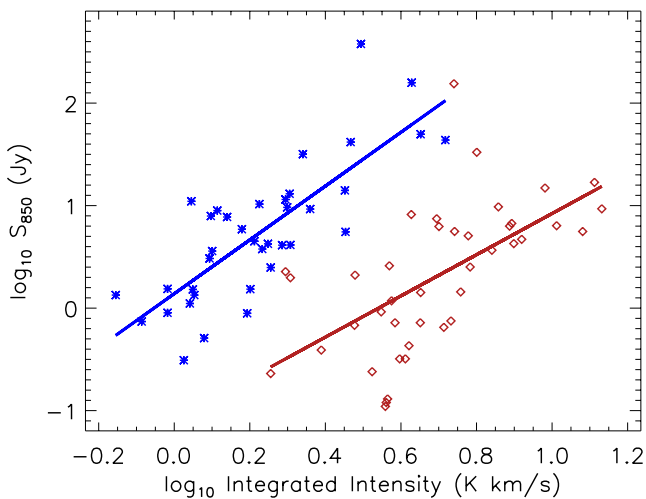
Figure 7. $\log_{10}$ integrated 850 µm fluxes versus NH$_3$ $\log_{10}$ integrated intensities for source associations in Perseus (red diamonds) and W3 (blue stars).
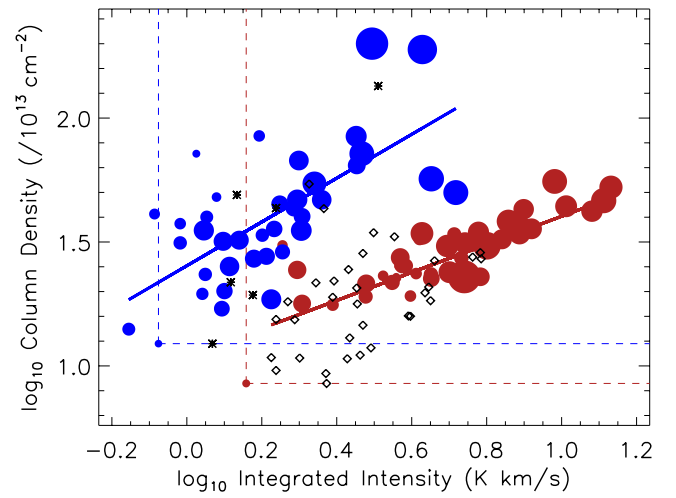
Figure 8. The distribution of ammonia column density against integrated intensity on a log–log scale. Circles represent submillimetre associations, the size of the circle representing the log value of the 850 µm integrated flux on a normalized scale. Blue and red circles represent sources in W3 and Perseus, respectively, stars (W3) and diamonds (Perseus) show the sources in those regions with no submillimetre association. Lines of best fit to all data points for each region are overlaid. Ammonia sensitivity limits are plotted as dashed lines with the 850 µm completeness estimate represented as a circle at the lower left corner.

in W3 are structurally similar to those in Perseus. Our findings are explained by either or both of two conclusions; one, that our sources are not well described by power-law intensity profiles. Two, that ammonia and submillimetre emission trace different structures, possibly related to different mass components.

In order to look for differences in source structure in the two star-forming regions, we compared the ratio of peak-to-integrated submillimetre flux densities for each source (hereafter $\eta_{\mathrm{int}}^{\mathrm{peak}}$). An object with an unresolved surface-brightness profile should present a $\eta_{\mathrm{int}}^{\mathrm{peak}}$ value approaching unity. Sources in the W3 sample typically have low values and a narrower distribution than in Perseus (Fig. 13). Mean values are 0.09 and 0.28 for W3 and Perseus, respectively. These results, combined with the derived filling factors (mean values of 0.12 and 0.42 in W3 and Perseus, respectively),
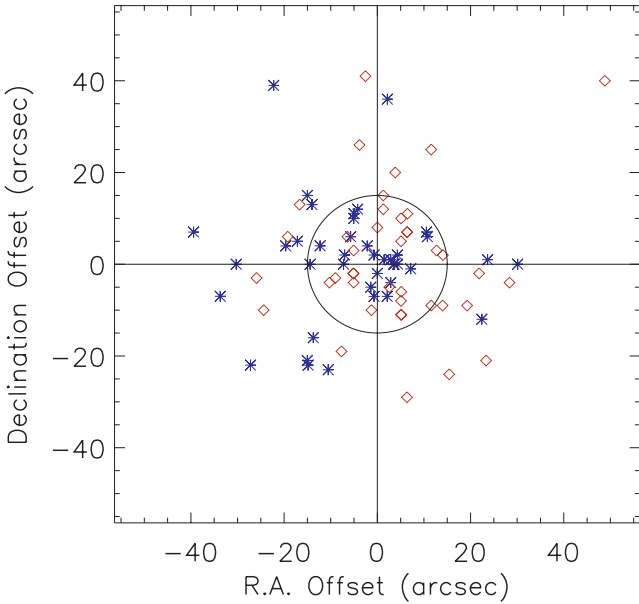
Figure 9. Offsets of the peak positions of each submillimetre source in Perseus (red diamonds) and W3 (blue stars) relative to the peak ammonia position centred at 0,0. The circle represents the radius of the GBT beam. Typical pointing errors in our observations are 4 arcsec.
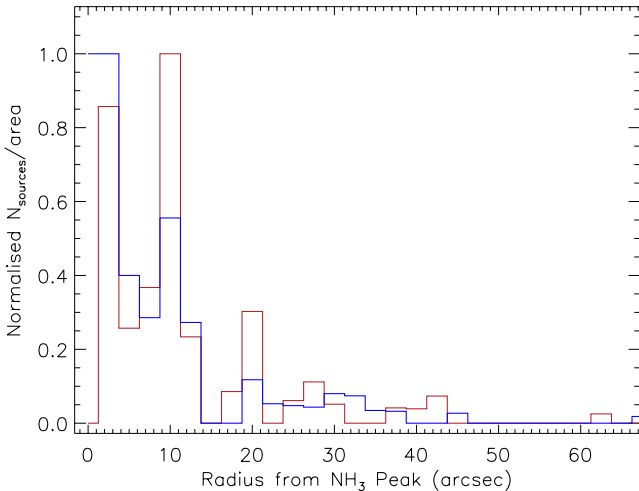

Figure 10. The surface density distribution of the offsets of peak positions of submillimetre sources related to the ammonia sources in Perseus (red) and W3 (blue).

provide information on the marginally resolved or unresolved structure of our sources. The higher values of η_{int}^{peak} in the Perseus sample indicate sources that are more compact than those in W3 and the low filling factors in W3, combined with low values of η_{int}^{peak}, indicate that these objects are extended but 'lumpy', with multiple sources within a beam. This explanation is consistent with the observation that each ammonia source in Perseus is typically associated with fewer submillimetre sources than in W3.

A more thorough examination of source structure, incorporating intensity profiles and the variation of ammonia and submillimetre emission in and around our sources will be more thoroughly examined in a following work (Morgan et al., in preparation).

3.5 The fractional abundance of ammonia

The fractional abundance of ammonia in protostellar clouds is a poorly defined quantity with estimates in specific regions varying from 7×10^{-10} (Di Francesco et al. 2002) to $\sim 1 \times 10^{-8}$ (Tafalla et al. 2004; Friesen et al. 2009). More recent values averaged over wide-field samples and Galactic plane surveys favour higher abundances with averages of $\sim 4 \times 10^{-8}$ (Dunham et al. 2011) and 1.2×10^{-7} (Wienen et al. 2012) found in single-pointing ammonia observations of the positions of peak surface brightness of sources detected in the thermal dust continuum at 1.1 mm (the Bolocam Galactic Plane Survey; Aguirre et al. 2011) and 870 μm (the Apex Telescope Large Area Survey of the Galaxy, ATLASGAL; Schuller et al. 2009), respectively. The abundance has also been shown to be dependent upon the internal structure of cores in some case studies (Tafalla et al. 2004). The apparent variation of ammonia abundance, both within cores and from source-to-source, means that the ammonia-derived gas mass is not a good estimator of total core mass, since it requires independent knowledge of the NH_3 abundance.

We have calculated the fractional abundance of ammonia for each source, both as an integrated property as well as within each source individually. The imperfect correlation of ammonia and submillimetre column density, as noted above, means that fractional abundances may only be determined for certain portions of many cores.

The abundance was calculated through the simple ratio of NH_3 column density to H_2 column density measured from submillimetre maps, where the latter were aligned and regridded to match the ammonia maps using a nearest neighbour interpolation. The H_2 column density is determined through the equation

$$N(H_2) = S_\nu \left[\Omega_m \mu m_H \kappa_\nu B_\nu(T_d) \right] \tag{1}$$

where S_ν represents the 850 μm flux density (evaluated per pixel), Ω_m is the main beam solid angle, μ is the mean molecular weight (taken as 2.29), m_H is the mass of a hydrogen atom and κ_ν is the dust opacity per unit mass at 850 μm, taken here and elsewhere as 0.01 cm^2 g^{-1}, in agreement with the OH5 model of Ossenkopf & Henning (1994). $B_\nu(T_d)$ represents the Planck function evaluated at a dust temperature T_d. We have taken T_d to be equal to the integrated NH_3 kinetic temperature over our sources. We are constrained in this choice mostly by a lack of options, a possible alternative being to simply select a single average dust temperature for all sources, a solution followed by many authors (e.g. Mitchell et al. 2001; Moore et al. 2007; Johnstone et al. 2010). We have used the approximation that $T_d \sim T_k$ as, first, we observe little variation of T_k over any given source (Morgan et al., in preparation). Secondly, the kinetic temperature of ammonia in star-forming sources has been found to be roughly equivalent to the dust temperature (see e.g. Morgan et al. 2010). These findings indicate that there is likely less error in the $T_d \sim T_k$ assumption than in the use of a single temperature for all sources.

It should be noted that we have used the temperature-averaging method described in Morgan et al. (2013) to extend our maps of ammonia column density for maximal coverage of the submillimetre emission. We find that fractional abundances of ammonia, averaged over each source, range from 7.9×10^{-8} to 2.7×10^{-7} in our Perseus sample (mean = 1.6×10^{-7}) and from 1.1×10^{-7} to 3.6×10^{-6} in W3 (mean = 6.2×10^{-7}). These values are likely to be prone to a high degree of uncertainty due to e.g. the ~ 50 per cent uncertainty in the estimated dust opacity, κ_ν (Shirley et al. 2011). We therefore estimate the uncertainty in abundance
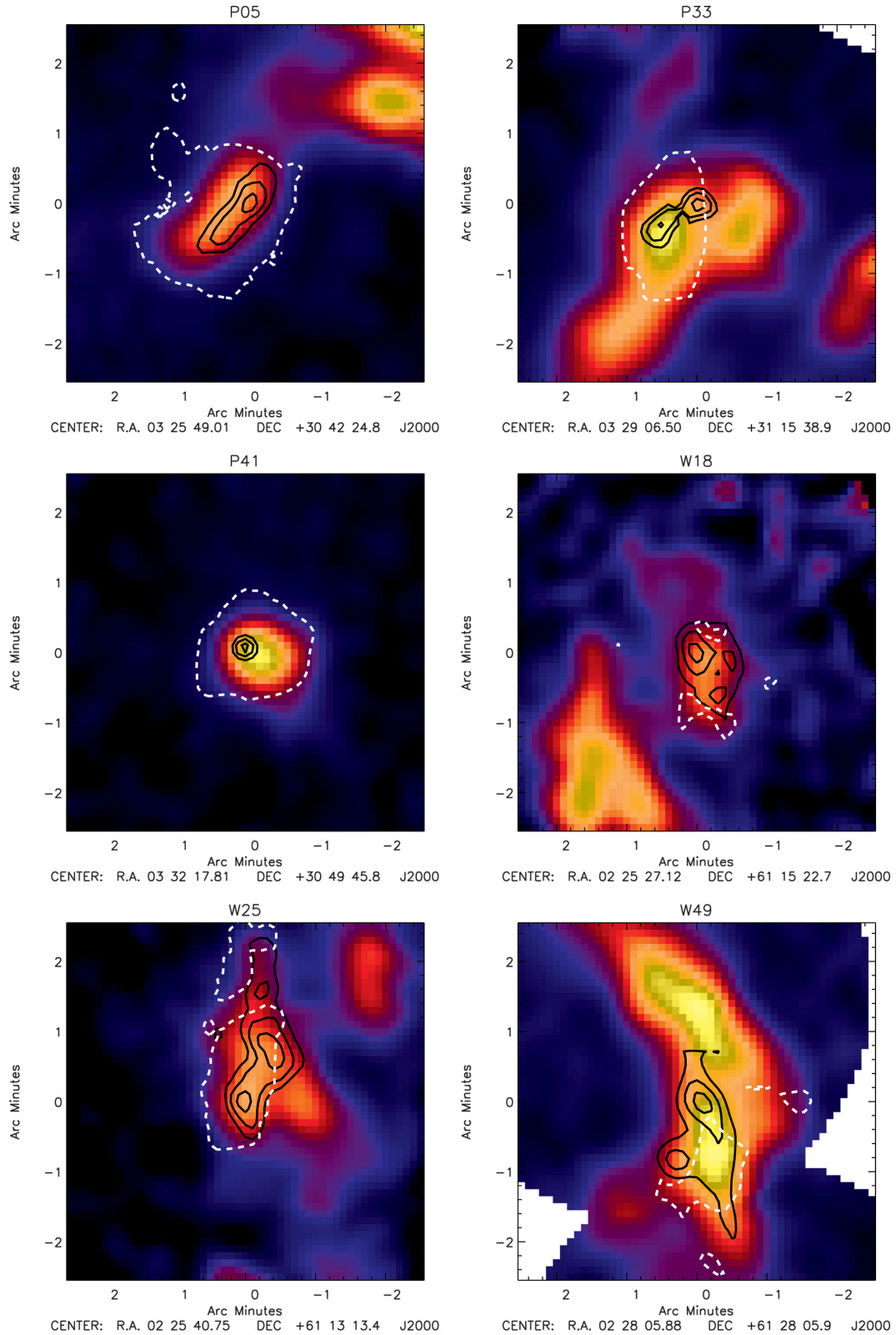
Figure 11. NH$_3$ integrated intensity in sources P05, P33 & P41 and W18, W25 & W49, overlaid with black contours of submillimetre emission at 50, 70 and 90 per cent of the peak flux density. A white, broken contour traces the NH$_3$ column density distribution at a level of 50 per cent of the local peak for all sources except W18, for which the contour level is 40 per cent. The full set of figures is available online.

Table 7. Source sizes in Perseus.

Perseus source	NH$_3$ $R_{\rm eff}$ (arcsec)	(pc)	Submillimetre $R_{\rm eff}$ (arcsec)	(pc)	Submillimetre $R_{\rm eff}$ NH$_3$ $R_{\rm eff}$
P01	27.4	0.035	20.8	0.026	0.76
P03	42.1	0.053	9.5	0.012	0.23
P05	40.7	0.051	26.4	0.033	0.65
P11	29.4	0.037	13.5	0.017	0.46
P13	45.4	0.057	23.5	0.030	0.52
P15	47.1	0.059	20.3	0.026	0.43
P22	31.8	0.040	11.0	0.014	0.35
P25	41.5	0.052	17.4	0.022	0.42
P26	31.5	0.040	12.6	0.016	0.40
P28	29.2	0.037	8.7	0.011	0.30
P30	32.0	0.040	9.7	0.012	0.30
P31	41.3	0.052	18.9	0.024	0.46
P32	40.8	0.051	20.2	0.025	0.50
P33	42.4	0.053	21.1	0.027	0.50
P34	47.0	0.059	29.4	0.037	0.63
P35	41.9	0.053	12.9	0.016	0.31
P36	38.1	0.048	16.9	0.021	0.44
P37	23.5	0.030	26.0	0.033	1.11
P40	27.1	0.034	12.8	0.016	0.47
P41	27.6	0.035	8.0	0.010	0.29
P47	38.8	0.049	37.1	0.047	0.96
P49	31.6	0.040	14.3	0.018	0.45
P50	42.1	0.053	23.4	0.029	0.56
P51	30.4	0.038	10.0	0.013	0.33
P52	37.0	0.047	13.3	0.017	0.36
P70	31.0	0.039	10.2	0.013	0.33
P71	50.7	0.064	24.0	0.030	0.47
P72	29.6	0.037	11.4	0.014	0.39
P73	32.7	0.041	16.9	0.021	0.52
P74	43.0	0.054	21.0	0.026	0.49
P75	33.1	0.042	22.9	0.029	0.69
P78	24.5	0.031	13.0	0.016	0.53
P80	23.0	0.029	9.9	0.012	0.43
Mean	35.6	0.045	17.2	0.022	0.49
Median	33.1	0.042	16.9	0.021	0.46
St. Dev.	7.5	0.010	6.9	0.009	0.19

Table 8. Source sizes in W3.

W3 source	NH$_3$ $R_{\rm eff}$ (arcsec)	(pc)	Submillimetre $R_{\rm eff}$ (arcsec)	(pc)	Submillimetre $R_{\rm eff}$ NH$_3$ $R_{\rm eff}$
W01	26.3	0.26	10.5	0.10	0.40
W02	28.6	0.28	30.0	0.29	1.05
W03	29.6	0.29	19.6	0.19	0.66
W06	32.7	0.32	22.7	0.22	0.69
W07	31.5	0.31	17.7	0.17	0.56
W08	35.7	0.35	26.2	0.25	0.73
W09	24.7	0.24	17.4	0.17	0.70
W10	27.8	0.27	46.4	0.45	1.67
W11	35.7	0.35	31.4	0.30	0.88
W12	22.3	0.22	20.9	0.20	0.94
W13	25.2	0.24	13.8	0.13	0.55
W14	19.2	0.19	19.4	0.19	1.01
W15	21.7	0.21	13.9	0.13	0.64
W17	18.3	0.18	46.6	0.45	2.55
W18	37.6	0.36	35.1	0.34	0.93
W19	34.6	0.34	44.0	0.43	1.27
W21	41.0	0.40	21.0	0.20	0.51
W22	36.9	0.36	38.8	0.38	1.05
W23	27.6	0.27	29.2	0.28	1.06
W25	45.8	0.44	52.2	0.51	1.14
W27	22.8	0.22	12.6	0.12	0.55
W28	23.8	0.23	26.5	0.26	1.11
W29	25.4	0.25	31.0	0.30	1.22
W30	37.4	0.36	26.0	0.25	0.70
W31	27.4	0.27	13.3	0.13	0.49
W33	52.6	0.51	41.8	0.41	0.79
W35/W38	30.6	0.30	52.1	0.51	1.70
W37	16.4	0.16	18.4	0.18	1.12
W39	36.6	0.35	13.6	0.13	0.37
W40	36.6	0.35	40.2	0.39	1.10
W43	9.8	0.10	16.6	0.16	1.69
W44	42.2	0.41	30.0	0.29	0.71
W45	21.7	0.21	33.1	0.32	1.53
W46	36.9	0.36	11.4	0.11	0.31
W48	54.7	0.53	53.2	0.52	0.97
W49	51.7	0.50	55.2	0.54	1.07
W50	54.8	0.53	58.2	0.56	1.06
W51	32.0	0.31	44.4	0.43	1.39
W52	37.9	0.37	38.4	0.37	1.01
W53	53.5	0.52	7.6	0.07	0.14
W54	23.5	0.23	12.6	0.12	0.54
Mean	32.5	0.31	29.1	0.28	0.94
Median	31.5	0.31	26.5	0.26	0.94
St. Dev.	10.9	0.11	14.4	0.14	0.46

values at 50 per cent, although we recognize the arbitrary nature of this estimate and the possibility that uncertainties may in fact be even higher. The distributions of abundance values for both Perseus and W3 cores are shown in Fig. 14. Despite the large uncertainty in individual abundance values, there is a large difference in the spread of the abundance distributions. A KS test of the distributions returns a 100 per cent probability that the samples are drawn from separate populations. The standard deviation of abundance values in Perseus is typically 29 per cent of the mean while, in W3, it is 98 per cent. In addition, the variation *within* individual cores is seen to be significantly higher in W3 than in Perseus with average standard deviations of 77 per cent and 39 per cent of the individual mean value, respectively.

It is common practice to estimate the fractional abundance of ammonia in star-forming regions through single-pointing observations directed at previously identified peaks of submillimetre emission (e.g. Rosolowsky et al. 2008; Dunham et al. 2011; Urquhart et al. 2011; Wienen et al. 2012). In order to test the assumption that measurements of ammonia abundance made at the position of dust emission peaks are representative of a given source, we compare the abundance found at the submillimetre peak position, $\chi_{\rm sm}$, with the average value over the entire source, $\overline{\chi}$. We define the quantity $\delta_\chi = [\chi_{\rm sm} - \overline{\chi}]/\overline{\chi}$. Fig. 15 shows the variation of δ_χ, the value of

ammonia abundance found at the position of peak submillimetre emission is significantly lower than the mean in all but one case and is not representative of the region as a whole. On average, the Perseus and W3 samples show similar values of δ_χ with mean differences of -52 per cent and -58 per cent, respectively, i.e. values of NH$_3$ abundance, at the position of peak submillimetre emission, are approximately a factor of 2 lower than the average for a given source. However, Fig. 15 shows that the distributions of δ_χ are skewed with the median in Perseus ($\widetilde{\delta_\chi} = -48$ per cent) higher than the mean. Conversely, the median in W3 ($\widetilde{\delta_\chi} = -65$ per cent) is lower than the mean. These results echo those of Friesen et al. (2009) in which they find that dust clumps in the region of Ophiuchus, as identified by 850 μm submillimetre emission, are associated with minima in the fractional abundance of ammonia. The possibility that this effect might be caused by the submillimetre peaks being coincident with
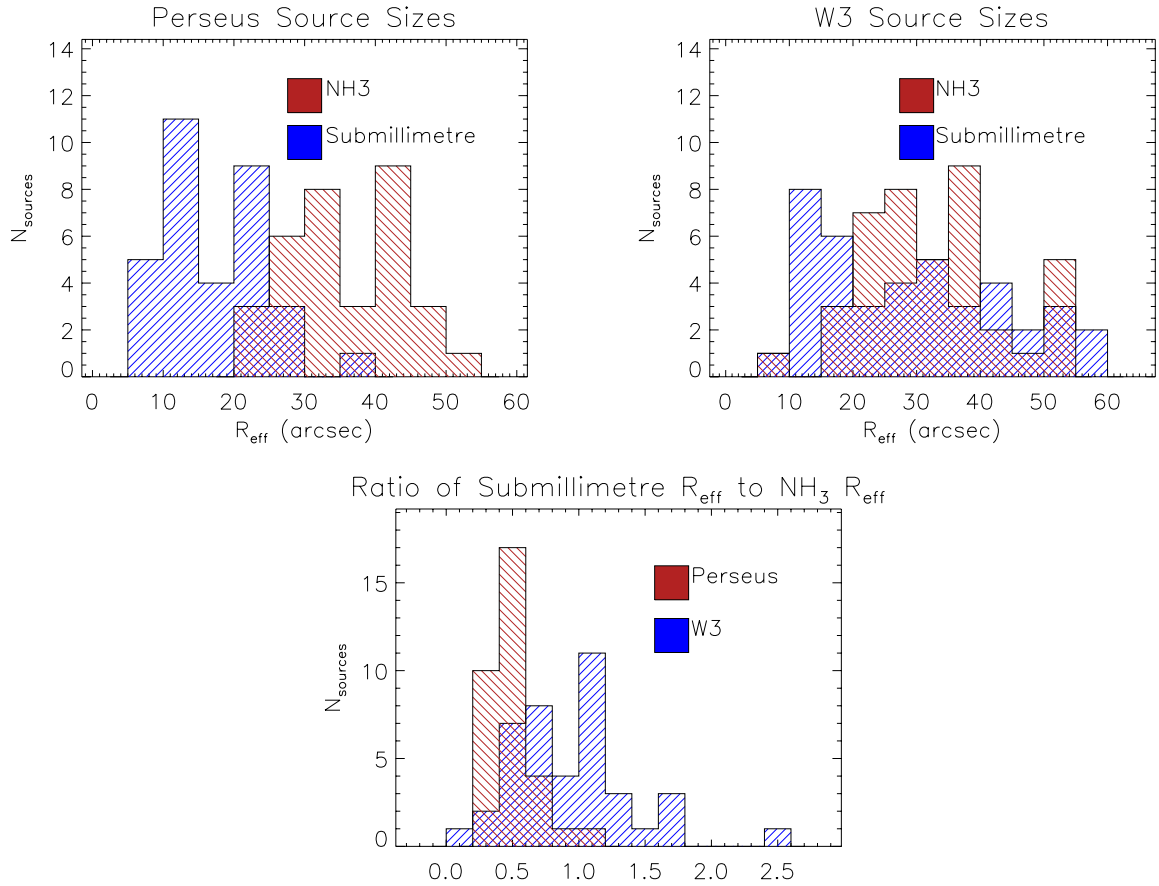
Figure 12. The distributions of submillimetre to ammonia source size ratios for Perseus (red) and W3 (blue).

Table 9. Convolved and regridded source sizes in Perseus.

Perseus Source	NH$_3$ R_{eff} (arcsec)	(pc)	Submillimetre R_{eff} (arcsec)	(pc)	Submillimetre R_{eff} NH$_3$ R_{eff}
Map01	11.9	0.12	7.7	0.07	0.65
Map02	22.8	0.22	10.3	0.10	0.45
Map07	18.7	0.18	7.8	0.08	0.42
Map08	23.1	0.22	6.0	0.06	0.26
Map09	18.0	0.17	16.1	0.16	0.89
Map10	10.4	0.10	8.9	0.09	0.86
Map11	14.9	0.14	8.5	0.08	0.57
Map12	18.3	0.18	10.5	0.10	0.57
Map13	14.5	0.14	8.6	0.08	0.59
P_b_1	16.0	0.16	9.6	0.09	0.60
P_b_2	20.7	0.20	8.8	0.09	0.43
Mean	17.2	0.17	9.4	0.09	0.57
Median	18.0	0.17	8.8	0.09	0.57
St. Dev	4.1	0.04	2.6	0.03	0.19

Figure 13. The distributions of peak to integrated flux ratios for submillimetre sources associated with our ammonia sources in Perseus (red) and W3 (blue).

dust temperature enhancements unresolved by the GBT beam was checked for by smoothing the submillimetre data to the resolution of the ammonia maps, resulting in similar results to the unsmoothed map analysis. Also, there is typically no evidence within our ammonia observations for kinetic temperature increases towards the peaks of submillimetre emission. Given the typical moderate-to-low optical depths of ammonia (1,1) line emission it seems unlikely that submillimetre emission is tracing temperature peaks that are unseen in our ammonia observations. However, it should be noted

that the lack of correlation between submillimetre peak positions and ammonia temperature does not take into account any variation of temperature within the clouds along the line of sight. If the submillimetre emission really is tracing higher temperatures towards embedded cores, then it is clear that these higher temperatures are not traced by the ammonia emission. It is also possible that gas and dust temperatures have become decoupled at scales below that of
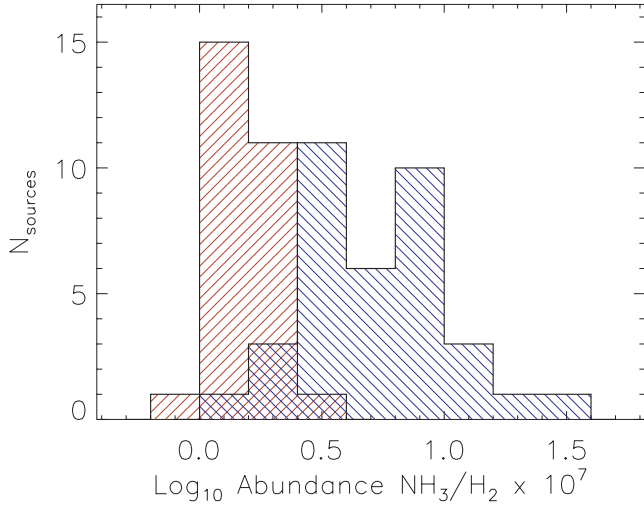
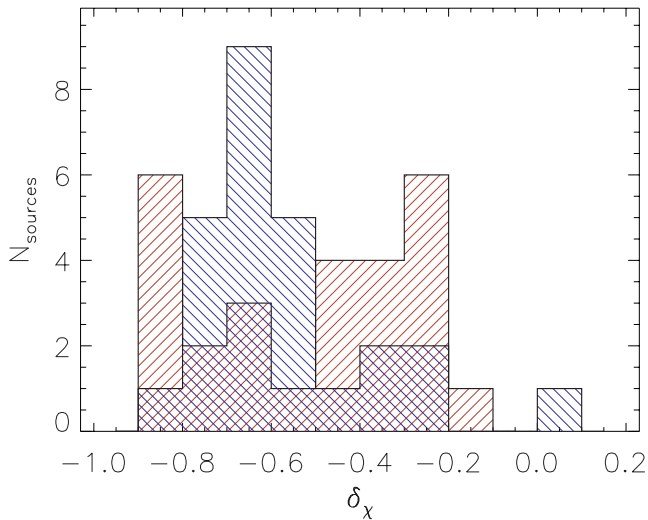**Figure 14.** NH₃ fractional abundances found in Perseus (red) and W3 (blue) cores.

Figure 15. Histogram plot of the difference in the fractional abundance at the submillimetre peak position compared to the mean found in Perseus (red) and W3 (blue) cores.

our observations, although this is thought to be unlikely in what are probably the highest density regions of the cores, where log (n) ∼ 5–6 (Myers & Fuller 1992).

It is particularly noteworthy that the median values of δ_χ are comparable to the standard deviations found for fractional abundance within individual cores, indicating that the practice of taking the position of peak submillimetre emission as representative of an entire source when measuring fractional abundance will lead to a bias greater than 1σ in a large proportion of cases.

3.6 Virial ratios

In order to further examine the nature of the observed sources in W3 in comparison to those in Perseus, we calculated the virial ratios of each source for which the necessary parameters had been obtained. Assuming spherical geometry and constant density we use the formulation

$$M_v = \frac{5 R_c \, \sigma_{V_{tot}}^2}{G} \qquad (2)$$
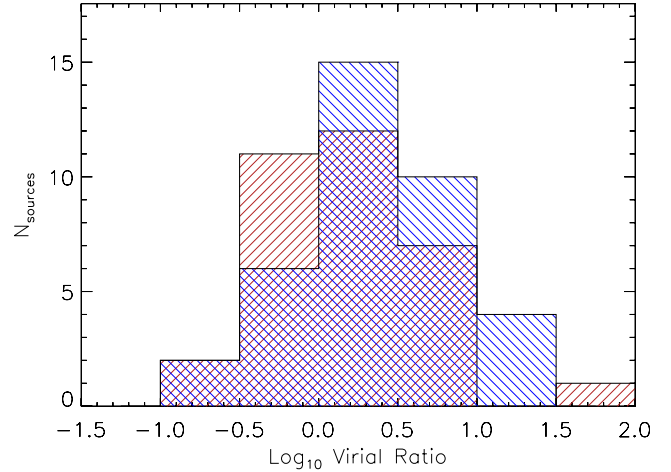
Figure 16. Number distribution plot of the log virial ratios found in the Perseus (red) and W3 (blue) regions.

to determine the virial mass of each core, where G is the gravitational constant and R_c is the submillimetre core radius as presented in Tables 7 and 8. $\sigma_{V_{tot}}$ is the 1D velocity dispersion integrated over the core in question, calculated by substituting the thermal contribution to the measured line width from ammonia with that assuming a mean molecular weight of 2.29 (i.e. $\sigma_{V_{tot}}^2 = \sigma_{V_{obs}}^2 - k_B T_k [\frac{1}{M_{NH_3}} - \frac{1}{2.29 M_H}]$). Having determined the virial mass of each core, we then calculated the virial ratio ($M_{observed}/M_v$) using the observed mass, determined using the submillimetre fluxes published by Moore et al. (2007) and Hatchell et al. (2007) and the kinetic temperatures determined from our ammonia observations; the resulting virial ratio values are plotted as a histogram in Fig. 16.

This approach requires the use of a mixture of NH₃ and sub-millimetre continuum data. The differing resolutions between these two types of observation in this study may introduce a bias in our values as larger physical regions are expected to exhibit greater turbulent linewidths (Larson 1981). As our observations of sources in W3 necessarily include greater amounts of material, turbulent linewidths are expected to be larger, thus increasing virial masses – some further discussion of this problem is presented in Section 4.1. Further, while molecular line data are necessary in order to determine velocity dispersion, submillimetre emission is our best tracer of core masses and radii, with the necessary assumption that they trace the same mass component. Since the column density match between NH₃ and submm continuum is not good in detail, this assumption is far from ideal and may introduce systematic biases or significant scatter into the results. The alternative would be to use NH₃-based masses and radii but this is likely to introduce even larger errors. In particular, core mass estimates from NH₃ data require an assumed NH₃ abundance, average values of which may be uncertain by orders of magnitude, as we have seen. Abundances in individual sources are more tightly constrained but are originally derived from submillimetre column densities. We are therefore obliged to use submillimetre continuum masses since they are more fundamental and so the submillimetre-traced core radii are also appropriate.

The results in Fig. 16 show significant and similar scatter in the virial ratios of our sources in both the Perseus and W3 regions. This scatter may be due in part to the uncertainties in determining virial ratio values. Estimates for submillimetre-derived mass require estimates of κ_ν, the frequency-dependent dust opacity per unit mass. This is highly uncertain with estimates varying from 0.01 cm² g⁻¹ (Moore et al. 2007) to 0.02 cm² g⁻¹ (Thompson et al. 2004), even

in similar regions. In addition to this, a significant uncertainty in mass ($\sim\sqrt{2}$; Morgan et al. 2008) can be attributed to temperature estimates through the Planck function. Therefore, we estimate uncertainties in virial ratio to be as large as 50 per cent. However, even this uncertainty cannot account for the scatter seen in virial ratios. This scatter is likely to be real, reflecting the physical state of the cores.

Median virial ratios for each region are 1.50 and 2.40 for Perseus and W3, respectively. Mean values are significantly higher at 3.50 and 4.50 which indicates a skew in both populations with tendencies to values above unity. The difference between the mean values is not large in comparison to the standard error at 1.46 and 0.90 for Perseus and W3, respectively. A KS test also shows no significant probability of the virial ratio values being drawn from separate populations at the 1 sigma level.

In the previous section, we described the effects on measured source sizes of convolving the Perseus data to lower resolution, in order to simulate observing it at the distance of W3. We have also examined the effect of this artificially reduced resolution on the apparent virial ratio for the 11 resulting convolved cores whose effective radii are listed in Table 9. The results show that the effect of reduced resolution, and so of greater distance, is to increase the apparent virial ratio of sources. In this case, the aggregated Perseus region sample has a significantly higher median virial ratio (4.2) than the native resolution Perseus sample. The explanation of this shift appears to be that the increase in mass included within the larger effective beam is greater than the corresponding increase in velocity dispersion.

4 DISCUSSION

4.1 General results

We find reasonable agreement between our results for ammonia sources in Perseus and those of Rosolowsky et al. (2008) who completed a single-pointing survey of ammonia observations, mainly towards submillimetre peaks in the Perseus region. A comparison of integrated intensity measurements at the positions of sources listed in Rosolowsky et al. (2008) shows that they are statistically indistinguishable. The median of the absolute difference between integrated intensity measurements of all matching sources is 13 per cent, consistent with expected uncertainties in our observational techniques.

In terms of the NH_3-derived source parameters, the average values and distributions show significant differences between the Perseus and W3 regions. In general terms these differences may be largely accounted for by the difference in distance between the two regions. Lower filling factors and optical depths are expected for regions at a greater distance due to the greater level of unresolved structure within our beam. Also, if core emission is extended, this may account for the differences seen in observed linewidth, with a greater amount of material being captured by the beam in W3 compared to Perseus, consistent with more sources being contained by the beam and/or a greater velocity dispersion associated with a greater scale of emission, as per the scaling relation of Larson (1981). The radii covered by the GBT beam correspond to 0.05 pc at the distance of Perseus and 0.31 pc at the distance of W3. This difference in physical scale means that there may be a distinct difference in the type of structure being traced in Perseus as compared to W3. However, it should be noted that the mean effective angular radii of our sources are approximately equal to our beam diameter in both Perseus and W3 (see Section 3.4), with R_{eff} measurements of 35.6 and 32.5 arcsec, respectively. This similarity in the angular scale

of the objects in our observations indicates that we may be tracing objects following power-law density profiles. For a power-law density profile in a given object the R_{eff}/FWHM ratio stays approximately constant between observations of varying resolution (Young et al. 2003), while for Gaussian-like or solid-disc density profiles this ratio will decrease approximately linearly. If the objects we are observing are hierarchical structures following a power-law density distribution (such as the commonly cited singular isothermal sphere model, which has a radial profile following $\rho \propto r^{-2}$ at all radii; Shu 1977), then the determined size of our objects may primarily depend upon the resolution and sensitivity of our observations. This dependence of source size upon the spatial distribution of matter, i.e. the density profile, may then directly relate to the variation we see in source size, as discussed in Section 3.4. The slope of the radial density profile may be important in moderately resolved sources (Terebey, Chandler & Andre 1993) and source size may equally be an indicator of the age of a source or the total source mass (Young et al. 2003). However, as a full analysis of core density distributions and other structure parameters is beyond the scope of the current work, this will be discussed in a forthcoming publication (Morgan et al., in preparation). A final point to be noted here is that convolution of the physical parameter maps derived from the Perseus data to a resolution comparable to that of W3 indicates that differences in distance are not able to explain the difference in physical parameters completely, resulting clump sizes are significantly smaller than native resolution observations, indicating that there is some real difference in the dense structures in the two regions, with larger clusters of objects in W3 than in Perseus. Higher average filling factors in the Perseus sample indicate that we are resolving the structure within Perseus to a finer level than within W3.

There are clear correlations between submillimetre and NH_3 detections (Section 3.4), although correlations in brightnesses of the two tracers are imperfect. The reasons for this are not clear; being reliably optically thin, submillimetre continuum emission has uncomplicated radiative transfer and thus is often considered a definitive tracer of column density. Line emission, conversely, has relatively complex radiative transfer and excitation processes requiring knowledge of or assumptions about optical depth and the relative population of energy levels.

83 per cent of the NH_3 sources in our combined W3 and Perseus catalogue, which have an associated submillimetre source, are found to contain at least one 22 μm source from the WISE catalogue (Wright et al. 2010) within their 50 per cent flux contour. These mid-IR associations likely indicate the presence of embedded protostars within the larger regions traced by ammonia and submillimetre continuum emission. However, it should be noted that the majority are offset from the position of peak submillimetre emission, with only 40 per cent of the WISE associations falling within a JCMT beam size (14 arcsec) of the measured position of the submillimetre peak.

The value of the fractional abundance of ammonia has been found to have a large range in the literature, with extreme values ranging over four orders of magnitude. Recent values over large self-consistent samples have considerable scatter within samples (see Dunham et al. 2011; Wienen et al. 2012) and, although there are well-established models which predict ammonia column density as a function of temperature (see Morgan et al. 2013), so far there is no well-established theory relating ammonia abundance with any physical parameter (e.g. density or temperature). Fractional abundance ratios found here by comparing integrated NH_3 and submillimetre-derived H_2 column densities are in a comparatively narrow range, within a range of a factor of 2 of the mean for sources in W3 and only 30 per cent in Perseus. These values are higher

by a factor between 2 and 10 than those generally found in the literature at $N_{NH_3}/N_{H_2} = \chi \sim 10^{-7}$ (cf. $\chi \sim 10^{-8}$; Tafalla et al. 2004; Friesen et al. 2009), though recent results based over large survey samples and with comparable resolution to our observations (Wienen et al. 2012; Dunham et al. 2011) are in better agreement. We find abundance ratios of ammonia to be considerably higher in W3 than in Perseus with a large degree of confidence, indicating that there is true variation of this metric from region to region. Given this, as well as the variation found within cores and the suggestion of an anti-correlation of submillimetre column density with ammonia abundance it is clear that determining NH_3 abundances using single-point data is not advisable. Also, when adopting abundance values to calculate total gas masses from NH_3 data, we must take account of the size scale under examination.

4.2 Association of gas and dust emission

In general, submillimetre sources are found to be associated with NH_3 emission. Submillimetre source peaks are found within NH_3 source boundaries and the detection rate of NH_3 associated with submillimetre cores is high. However, the correlation between the two tracers is not overly strong; there are many ($\sim$40 per cent) sources for which peaks in NH_3 and submillimetre emission do not coincide (cf. the study of Friesen et al. 2009 of the Ophiuchus region) and the overall contours of emission are poorly correlated in a significant number of sources. In addition, an anti-correlation exists between peaks of the column density measured through submillimetre emission and the fractional abundance of ammonia (see Section 3.5) with the anti-correlation stronger on average in our W3 sample than for sources in Perseus. Relative abundances at the position of maximum column density are consistently lower than the average over the whole core for most of our sources, implying that the NH_3 traced column distributions are flatter than the submm ones, even when smoothed to a matching resolution. The relationship of fractional abundance of ammonia to submillimetre column density is complex as, not only may the dust opacity factor (κ_ν) inherent in the derivation of submillimetre column density vary from region-to-region, it may actually vary considerably within regions.

The number of sources which have a weak correlation between their position of emission peaks for submillimetre continuum and ammonia emission has a possible explanation in terms of temperature gradients. Derived column densities derived from submillimetre and ammonia emission depend in opposite ways upon the assumed temperature, with a direct dependence in the ammonia case and an inverse relationship for the continuum (for a fixed intensity). Column density measurements made from submillimetre observations are dependent upon temperature estimates through the Planck function and are therefore quite strongly subject to errors in the assumed T. However, measurements of the error in column density compared to errors in T indicate that the relationship is linear for temperatures around the mean found in our observations (13.14 K and 18.50 K for Perseus and W3, respectively), with a 20 per cent error in T translating to 29 per cent and 20 per cent errors in column density for Perseus and W3, respectively.

The lack of detailed correlation (and particularly the dips seen in ammonia fractional abundance towards submillimetre peaks) may be explained by undetected peaks in the temperature distribution. While a full analysis of the spatial variation of various physical parameters measured from our ammonia observations (temperature, linewidth, etc.) is left for a separate study, kinetic temperature distributions generally show minima at the submillimetre continuum emission peaks, rather than maxima. Any undetected local temper-

ature rises must therefore be negligible on the scales probed by the current data. Also, the 22 µm WISE sources which we observe in and around our sources, which we might expect to trace internally heated protostellar cores, show considerable positional scatter around both the submillimetre and ammonia T_k peaks. This indicates that, while the presence of the WISE source is likely to indicate a peaked temperature distribution, this is not traced by either our ammonia observations or the thermal emission at the scale at which we can resolve that emission. We suggest that the 22 µm sources are likely tracing more evolved star formation than the submillimetre and/or ammonia emission.

Our results imply that NH_3 emission and the submillimetre continuum do not reliably trace the same mass component in detail, suggesting variations in excitation conditions (i.e. temperature or density) on scales smaller than the beam or deviations from LTE within cores. Explicitly, an inequality of dust and gas temperatures invalidates the assumption of thermal coupling between the gas and dust, while mis-assigned temperatures create disproportionate errors in gas/dust associations. This is likely to be particularly relevant when determining fractional abundances of ammonia. In the case that densities in the observed regions are lower than the critical density of ammonia ($\sim$4 $\times$ 10^3 cm^{-3}; Maret et al. 2009) and NH_3 is sub-thermally excited then we may expect NH_3 emission to be fainter than predicted in a LTE analysis and so low-density sources may be responsible for the submillimetre sources we find with no corresponding ammonia detection.

There are multiple chemical effects which potentially have a bearing on our study. First, the NH_3 molecule is, like all molecules, subject to depletion in dense, cold gas by freezing out of the gas phase on to the surfaces of dust grains. This has the effect of significantly altering the abundance in a somewhat unpredictable way, though nitrogen-bearing molecules such as NH_3 are usually predicted by models to be slow to freeze out, even at high densities (Bergin & Langer 1997; Charnley 1997). Secondly, the presence (or absence) of CO in star-forming cores has a significant effect on less abundant species (Lee, Bergin & Evans 2004), including ammonia due to the interaction between freezeout and evaporation of the molecules themselves and CO. The competition between 'freeze-out' and CO evaporation in an internally heated core is significant when determining the abundance of N_2H^+ and NH_3. However, these are largely confined to a small radius (see Lee et al. 2004). Recent models which invoke episodic accretion provide an estimate of the zone of CO evaporation and ammonia destruction (Kim et al. 2012). Using spectral energy distribution determinations for protostellar cores in Perseus (Dunham et al. 2013) we find a median extinction corrected bolometric luminosity of 1.20 L$_\odot$ (with a range of 0.05 to 37 L$_\odot$). From fig. 3 of Kim et al. (2012) we can use these values to estimate the radius at which cores in Perseus reach the evaporation temperature of CO ($\sim$25 K; Lee et al. 2004) – this is approximately 500–600 au for a 1.2 L$_\odot$ core, increasing to $\sim$2000 au for the maximum luminosity of 37 L$_\odot$ which was determined. These radii are considerably below the resolution of our ammonia observations with a GBT full width at half-maximum beam size of $\sim$8300 au at the distance of the Perseus molecular cloud.

While there are physical reasons relating to temperature gradients and protostellar chemistry why we may not observe strong correlations between ammonia and submillimetre continuum emission peaks and why there is a prevalent anti-correlation of the fractional abundance of ammonia towards submillimetre emission peak, these are hard to reconcile with the observations that we have presented, potentially due to the physical scale which these observations are sampling.

4.3 Virial ratio

In Section 3.6, we described the determination of virial ratios for each region. The distribution of virial ratios in the two samples is similar, though with a lower median in Perseus than in W3. There are a significant number of sources with values of virial ratios indicating unbound objects; these may represent cores which have formed stars and started to be disrupted, or where the bound part of the core has collapsed and disappeared from the gas and dust tracers but its gravitational potential energy remains.

Differences seen in virial ratio values between the two regions in our sample may be understood in terms of a structural difference. The spatial resolution of our ammonia observations (0.04 pc and 0.29 pc for Perseus and W3, respectively) is such that we may well be selecting sources which will result in the formation of multiple stars and, while we have generally described our sources as 'cores' (the precursors of single stars or small binary systems), the presence of multiple 22 μm sources indicates that they might be more correctly referred to as 'clumps' (overdense regions out of which stellar clusters form; McKee & Ostriker 2007). Further, the analysis of our ammonia maps shows several sources that exhibit filamentary structure (e.g. P35 and W11). This is likely to have stronger repercussions for our analysis of the W3 region than for Perseus, given the larger spatial scale we are examining in W3. We have attempted to account for this through the convolution of our Perseus observations to mimic the distance of the W3 region, resulting in higher virial ratios for our convolved sources than even the native resolution W3 observations. This implies that the value of virial ratio found for a given source is a function of spatial resolution. A more physical interpretation is that star-forming clumps are bound on large scales but cores are pressure-confined on smaller scales although these possibilities are not mutually exclusive.

We have suggested several times in this work that an inherent difference in the physical structure of the Perseus and W3 regions may be responsible for some of the observed differences we have described (see Section 4.1). Myers (2013) presents a model in which low-mass cores draw mass from inner filament gas in their formation, while higher-mass cores draw from the more extended filament gas. Assuming that our observations are of an appropriate scale in both regions, this model would provide some explanation for our results in that, for Perseus, virial ratios are based upon linewidths taken from the more extended gas which we do not expect to form part of the final stellar product. In W3, this more extended material is part of the bound structure, possibly resulting in higher virial ratio values (though this might be expected to be offset by higher velocity dispersions). For this interpretation to be correct, we expect that the submillimetre observations are tracing the compact 'core' structure in both regions, while the ammonia traces the more extended, filamentary material.

5 SUMMARY AND CONCLUSIONS

This study was designed to assess the way in which observable parameters associated with gas and dust emission are related, a further goal was to compare those results between a region of high-mass star formation and a region of low-mass star formation. In terms of source brightness, our observations of ammonia in the Perseus and W3 star-forming regions are consistent with previous observations, with differences explainable by measurement error.

There are clear differences in the measured physical parameters of dense cores in the Perseus and W3 samples. Most of these differences can be attributed to resolution effects introduced by the considerably larger distance of the W3 cloud. For example, lower filling factors in W3 indicate additional structure within the beam and larger linewidths are expected from larger scale emission. Several parameter differences are not so easily explained this way, however. Source sizes in the Perseus data are significantly smaller than in W3, even when convolved to compensate for distance, indicating real differences in source structure between the two regions, with individual cores more likely to be traced within Perseus and larger clusters of objects or filaments being traced in W3.

A general correlation of submillimetre and ammonia emission has led to many studies using the two tracers in combination to derive, e.g. NH_3 fractional abundances and virial ratios. However, we have shown that the correlation is imperfect in detail, with significant scatter in the positions of peak surface brightness and an anti-correlation of submillimetre-traced column density and differential NH_3 abundance within individual cores. This shows that a full understanding of the relationship of ammonia to the cold dust component traced by submillimetre emission is yet to be attained and that mapping of NH_3 emission is preferable to single-pointing measurements for determination of integrated source physical parameters.

Although a comparison of ammonia sources to submillimetre emission reveals that sensitivity limitations may be responsible for certain sources being detected in one tracer but not the other, the lack of detailed correlation between the emission features of NH_3 and submillimetre continuum may also indicate variations in NH_3 abundance or excitation conditions within star-forming cores. For example, we see that ammonia temperature dips towards the position of peak submillimetre emission, indicating that the two tracers are not necessarily thermally coupled and that ammonia may well be cooled through efficient cooling in regions of high density. While ongoing star formation is indicated in the general environment of our catalogue through the presence of 22 μm IR sources, these are only coincident with peaks of submillimetre emission in a minority. Overall, our source catalogue then appears to consist primarily of prestellar or early protostellar cores which are likely still undergoing infall. The anti-correlation between NH_3 abundance and submillimetre-traced column density within cores varies in significance and slope between the Perseus and W3 regions, with a stronger correlation and steeper slope in Perseus. Depletion models of ammonia do not describe a situation easily applied to our observations and this phenomenon requires further study.

Virial ratios were found to be higher in the W3 sources than for sources in Perseus. However, we also find that, by artificially placing Perseus cores at an equivalent distance to W3 by degrading the resolution, the virial ratios are increased. These results may indicate a selection effect, but may also indicate a difference in the underlying structure and physics of the two star-forming regions, dependent upon their relative mass.

have been possible without the SIMBAD astronomical data base service operated at CDS, Strasbourg, France and the NASA Astrophysics Data System Bibliographic Services.

REFERENCES

Aguirre J. E. et al., 2011, ApJS, 192, 4

Allsopp J., 2012, PhD thesis, Liverpool John Moores University

Bergin E. A., Langer W. D., 1997, ApJ, 486, 316

Charnley S. B., 1997, MNRAS, 291, 455

Chira R.-A., Beuther H., Linz H., Schuller F., Walmsley C. M., Menten K. M., Bronfman L., 2013, A&A, 552, A40

Curtis E. I., Richer J. S., 2010, MNRAS, 402, 603

Di Francesco J., Hogerheijde M. R., Welch W. J., Bergin E. A., 2002, AJ, 124, 2749

Dunham M. K., Rosolowsky E., Evans N. J. II, Cyganowski C., Urquhart J. S., 2011, ApJ, 741, 110

Dunham M. M. et al., 2013, AJ, 145, 94

Enoch M. L. et al., 2006, ApJ, 638, 293

Enoch M. L., Glenn J., Evans N. J. II, Sargent A. I., Young K. E., Huard T. L., 2007, ApJ, 666, 982

Friesen R. K., Di Francesco J., Shirley Y. L., Myers P. C., 2009, ApJ, 697, 1457

Hatchell J., Richer J. S., Fuller G. A., Qualtrough C. J., Ladd E. F., Chandler C. J., 2005, A&A, 440, 151

Hatchell J., Fuller G. A., Richer J. S., Harries T. J., Ladd E. F., 2007, A&A, 468, 1009

Ho P. T. P., Townes C. H., 1983, ARA&A, 21, 239

Johnstone D., Rosolowsky E., Tafalla M., Kirk H., 2010, ApJ, 711, 655

Keto E., Caselli P., 2008, ApJ, 683, 238

Kim H. J., Evans N. J., II, Dunham M. M., Lee J.-E., Pontoppidan K. M., 2012, ApJ, 758, 38

Lada C. J., Elmegreen B. G., Cong H.-I., Thaddeus P., 1978, ApJ, 226, L39

Landsman W. B., 1993, in Hanisch R. J., Brissenden R. J. V., Barnes J., eds, ASP Conf. Ser. Vol. 52, Astronomical Data Analysis Software and Systems II., Astron. Soc. Pac., San Francisco, p. 246

Larson R. B., 1981, MNRAS, 194, 809

Lee J.-E., Bergin E. A., Evans N. J., II, 2004, ApJ, 617, 360

McKee C. F., Ostriker E. C., 2007, ARA&A, 45, 565

Maret S., Faure A., Scifoni E., Wiesenfeld L., 2009, MNRAS, 399, 425

Mitchell G. F., Johnstone D., Moriarty-Schieven G., Fich M., Tothill N. F. H., 2001, ApJ, 556, 215

Moore T. J. T., Bretherton D. E., Fujiyoshi T., Ridge N. A., Allsopp J., Hoare M. G., Lumsden S. L., Richer J. S., 2007, MNRAS, 379, 663

Morgan L. K., Thompson M. A., Urquhart J. S., White G. J., 2008, A&A, 477, 557

Morgan L. K., Figura C. C., Urquhart J. S., Thompson M. A., 2010, MNRAS, 408, 157

Morgan L. K., Moore T. J. T., Allsopp J., Eden D. J., 2013, MNRAS, 428, 1160

Myers P. C., 2013, ApJ, 764, 140

Myers P. C., Fuller G. A., 1992, ApJ, 396, 631

Ossenkopf V., Henning T., 1994, A&A, 291, 943

Pineda J. E., Rosolowsky E. W., Goodman A. A., 2009, ApJ, 699, L134

Reid M. A., Wadsley J., Petitclerc N., Sills A., 2010, ApJ, 719, 561

Rosolowsky E. W., Pineda J. E., Foster J. B., Borkin M. A., Kauffmann J., Caselli P., Myers P. C., Goodman A. A., 2008, ApJS, 175, 509

Schuller F. et al., 2009, A&A, 504, 415

Shirley Y. L., Huard T. L., Pontoppidan K. M., Wilner D. J., Stutz A. M., Bieging J. H., Evans N. J., II, 2011, ApJ, 728, 143

Shu F. H., 1977, ApJ, 214, 488

Smith R. J., Clark P. C., Bonnell I. A., 2008, MNRAS, 391, 1091

Tafalla M., Myers P. C., Caselli P., Walmsley C. M., 2004, Ap&SS, 292, 347

Terebey S., Chandler C. J., Andre P., 1993, ApJ, 414, 759

Thompson M. A., White G. J., Morgan L. K., Miao J., Fridlund C. V. M., Huldtgren-White M., 2004, A&A, 414, 1017

Tieftrunk A. R., Megeath S. T., Wilson T. L., Rayner J. T., 1998, A&A, 336, 991

Urquhart J. S. et al., 2011, MNRAS, 418, 1689

Ward R. L., Wadsley J., Sills A., Petitclerc N., 2012, ApJ, 756, 119

Wienen M., Wyrowski F., Schuller F., Menten K. M., Walmsley C. M., Bronfman L., Motte F., 2012, A&A, 544, A146

Williams J. P., de Geus E. J., Blitz L., 1994, ApJ, 428, 693

Wilson T. L., Gaume R. A., Johnston K. J., 1993, ApJ, 402, 230

Wright E. L. et al., 2010, AJ, 140, 1868

Young C. H., Shirley Y. L., Evans N. J. II, Rawlings J. M. C., 2003, ApJS, 145, 111

Zeng Q., Hermsen W., Wilson T. L., Batrla W., 1984, A&A, 140, 169

Zhou S., Evans N. J. II, Guesten R., Mundy L. G., Kutner M. L., 1991, ApJ, 372, 518

SUPPORTING INFORMATION

Additional Supporting Information may be found in the online version of this article:

Figure 11. The full set of NH_3 integrated intensity maps. (http://mnras.oxfordjournals.org/lookup/suppl/doi:10.1093/mnras/stu362/-/DC1)

Please note: Oxford University Press is not responsible for the content or functionality of any supporting materials supplied by the authors. Any queries (other than missing material) should be directed to the corresponding author for the article.

This paper has been typeset from a TEX/LATEX file prepared by the author.